

Physical Properties of Fullerene-containing Galactic Planetary Nebulae

Masaaki Otsuka^{1*}, F. Kemper¹, J. Cami^{2,3}, E. Peeters^{2,3}, J. Bernard-Salas^{4,5}

¹*Institute of Astronomy and Astrophysics, Academia Sinica, 11F of Astronomy-Mathematics Building, AS/NTU. No.1, Sec. 4, Roosevelt Rd, Taipei 10617, Taiwan, R.O.C.*

²*Department of Physics and Astronomy, The University of Western Ontario, London, ON N6A 3K7, Canada*

³*SETI Institute, 189 Bernardo Ave, Suite 100, Mountain View, CA 94043, USA*

⁴*Institut d'Astrophysique Spatiale, CNRS/Université Paris-Sud 11, 91405 Orsay, France*

⁵*current address: Department of Physical Sciences, The Open University, Milton Keynes, MK7 6AA, UK*

ABSTRACT

We searched the *Spitzer* Space Telescope data archive for Galactic planetary nebulae (PNe), that show the characteristic 17.4 and 18.9 μm features due to C_{60} , also known as buckminsterfullerene. Out of 338 objects with *Spitzer*/IRS data, we found eleven C_{60} -containing PNe, six of which (Hen2-68, IC2501, K3-62, M1-6, M1-9, and SaSt2-3) are new detections, not known to contain C_{60} prior to this work. The strongest 17.4 and 18.9 μm C_{60} features are seen in Tc 1 and SaSt 2-3, and these two sources also prominently show the C_{60} resonances at 7.0 and 8.5 μm . In the other nine sources, the 7.0 and 8.5 μm features due to C_{60} are much weaker. We analyzed the spectra, along with ancillary data, using the photo-ionization code CLOUDY to establish the atomic line fluxes, and determine the properties of the radiation field, as set by the effective temperature of the central star. In addition, we measured the infrared spectral features due to dust grains. We find that the Polycyclic Aromatic Hydrocarbon (PAH) profile over 6-9 μm in these C_{60} -bearing carbon-rich PNe is of the more chemically-processed class A. The intensity ratio of 3.3 μm to 11.3 μm PAH indicates that the number of C-atoms per PAH in C_{60} -containing PNe is small compared to that in non- C_{60} PNe. The *Spitzer* spectra also show broad dust features around 11 and 30 μm . Analysis of the 30- μm feature shows that it is strongly correlated with the continuum, and we propose that a single carbon-based carrier is responsible for both the continuum and the feature. The strength of the 11- μm feature is correlated to the temperature of the dust, suggesting that it is at least partially due to a solid-state carrier. The chemical abundances of C_{60} -containing PNe can be explained by AGB nucleosynthesis models for initially 1.5-2.5 M_{\odot} stars with $Z=0.004$. We plotted the locations of C_{60} -containing PNe on a face-on map of the Milky Way and we found that most of these PNe are outside the solar circle, consistent with low metallicity values. Their metallicity suggests that the progenitors are an older population.

Key words: ISM: planetary nebulae:general — ISM:molecules — ISM:dust,extinction

1 INTRODUCTION

Since their laboratory discovery in 1985 (Kroto et al. 1985), fullerenes, particularly C_{60} , have drawn considerable interest from astrochemists looking for them in interstellar conditions. Fullerenes are extremely stable and easily form in laboratories on the earth, so it had been thought that they should exist in interstellar space. However, the first confirmed detection of cosmic fullerenes was only recently reported by Cami et al. (2010) in the C-rich planetary nebula (PN) Tc1. Since then, a plethora of papers reported the discovery of cosmic fullerenes in Galactic (García-Hernández et al. 2010, 2011a; Otsuka et al. 2013; Zhang & Kwok 2011) and Large/Small Magellanic PNe

(García-Hernández et al. 2010, 2011a), Galactic asymptotic giant branch (AGB) stars (Gielen et al. 2011), H-poor R Coronae Borealis (R CrB) stars (García-Hernández et al. 2011b; Clayton et al. 2011), reflection nebulae (Sellgren et al. 2010; Peeters et al. 2012), a binary XX Oph star (Evans et al. 2012), and YSOs (Roberts et al. 2012). While the number of fullerene detections is increasing, the formation process and the excitation mechanism of fullerenes in evolved stars are the subject of active research. For instance, a recent work of Micelotta et al. (2012) details a possible formation mechanism, while Bernard-Salas et al. (2012) provides an observational/theoretical study of the fullerene excitation conditions. In order to allow for further investigation of the formation and excitation mechanisms, it is of crucial importance to characterize the observational and physical properties of the environments in which

* E-mail:otsuka@asiaa.sinica.edu.tw

fullerenes are found. PNe provide an excellent opportunity to do this.

PNe represent the final stage in the evolution of initially 1-8 M_{\odot} stars. At the end of its life, such a star evolves first into a red giant branch star, then an AGB star, finally a PN. In the early AGB stage, dust grains are formed above the surface of the star. Dust grains receive radiation pressure from the central star and move radially outward. The grains drag the H-rich envelope; as a result, dramatic mass-loss begins. Dust controls not only the mass-loss history of the stars but also the evolution of the ISM in galaxies. To understand the stellar evolution and the ISM evolution in galaxies, it is important to understand the amount, composition, formation process of the dust grains produced by dying stars.

According to stellar evolution theory, stars with a main-sequence mass $\sim 1.2\text{-}3.5 M_{\odot}$ can efficiently synthesize C by nucleosynthesis taking place in the He-rich intershell and the third dredge-up during the late AGB phase, so that these stars evolve into C-rich AGB stars/PNe. Several species of C-rich dust can form in the ejected nebula. Using infrared space telescopes such as *ISO*, *Spitzer*, and *AKARI*, the presence of these dust species was confirmed using the characteristic emission bands in mid-infrared spectra in the range from ~ 3 to $\sim 40 \mu\text{m}$; for example, amorphous carbon, polycyclic hydrocarbon (PAH), the $11 \mu\text{m}$ silicon carbide (SiC) band, and the unidentified $30 \mu\text{m}$ feature are detected. C-rich evolved stars are important producers of C based dust grains in galaxies.

In order to address the outstanding questions on the formation and the excitation mechanism of C_{60} in evolved stars, in particular, PNe, it is necessary to find more fullerene containing PNe in the entire *Spitzer* data archive, measure the C_{60} band as accurately as possible, and investigate the properties of dust, ionized gas, and central stars in these C_{60} -containing PNe.

In this paper, we present results that are based on *all* *Spitzer*/IRS observations of Galactic PNe (338 objects in total). Our search resulted in six new detections: Hen2-68, IC2501, K3-62, M1-6, M1-9, and SaSt2-3. In addition, we found the 17.4 and 18.9 μm C_{60} bands in the *Spitzer*/IRS SH spectrum of IC418; Morisset et al. (2012) reported the C_{60} detection in *ISO* spectra. We compare the *Spitzer*, *AKARI*, and *ISO* mid-IR spectra of these objects and previously known fullerene-containing PNe M1-11 (Otsuka et al. 2013), M1-12, M1-20 (García-Hernández et al. 2010), and Tc1 (Cami et al. 2010) to the properties of the central stars and the other dust features such as the 3.3 and the 6-9 μm PAH bands, the broad 11 μm and 30 μm features, which are frequently seen in C_{60} PNe. Moreover, we construct photo-ionization models using *CLOUDY* (Ferland et al. 1998) to derive the physical properties of the central stars and the nebulae of the eleven PNe in our sample.

2 OBSERVATIONS & DATA REDUCTION

Our aim is to study in detail the properties of the gas and dust in Galactic fullerene-containing PNe, to provide constraints on C_{60} formation and excitation, and to find clues to the formation and processing of carbonaceous dust. Mid-infrared observations at high spectral resolution are crucial for this, and we thus selected our sample based on the availability of the *Spitzer*/IRS SL (5.2-14.5 μm), SH (9.9-19.6 μm), and LH (18.7-37.2 μm) spectra and *ISO* spectra. Where available, we have also included data at shorter wavelengths from *AKARI*/IRC 2.5-5 μm spectroscopy, as well as optical and infrared images from the Hubble Space Tele-

Table 2. The flux density at the *WISE* band 4 and the adopted scaling factor for *Spitzer*/IRS and *ISO*.

Nebula	$F_{\nu}(\text{WISE4})$ (Jy)	Scaling Factor
Hen2-68	4.34	1.288
IC418	150.33	1.203
IC2501	19.40	2.519 ^a
K3-62	9.56	1.215
M1-6	9.10	1.251
M1-9	1.36	1.081
M1-11	52.51	1.181
M1-12	9.13	1.224
M1-20	3.17	1.257
SaSt2-3	0.242	1.147
Tc1	10.08	3.858

^adetermined using the 2MASS *Ks* image. See text for detail.

scope (*HST*), the 8.2-m Gemini telescopes, and the ESO/NTT 3.6-m telescope to get a better understanding of the properties of gas and dust.

The observation logs for *Spitzer*, *ISO*, and *AKARI* are summarized in Table 1. The second column is the position of each PN in the Galactic coordinates. The information of *Spitzer* and *ISO* observations is summarized in the third to sixth columns. The signal-to-noise ratios (SNR) are measured between 18.5 and 19.5 μm for *Spitzer* and *ISO*/SWS and between 148 and 154 μm for *ISO*/LWS spectra, respectively. The information of *AKARI*/IRC observations are in the remaining columns. The SNRs are measured between 3.3 and 3.6 μm .

2.1 *Spitzer*-IRS and *ISO* spectra

We searched the entire *Spitzer* Infrared Spectrograph (IRS, Houck et al. 2004) archive for PNe with observations in the SL (5.2-14.5 μm), SH (9.9-19.6 μm), and LH (18.7-37.2 μm) modules. In this search, we found six new fullerene-containing PNe, namely, Hen2-68, IC2501, K3-62, M1-6, M1-9, and SaSt2-3. Morisset et al. (2012) reported that IC418 shows two resonances at 17.4 and 18.9 μm in the *ISO* spectra due to C_{60} . We confirmed both of these C_{60} lines in the *Spitzer* spectrum of IC418, which was not previously analyzed. We combine this data set with *Spitzer*/IRS spectra of M1-11, M1-12, M1-20, and Tc1, which are known to show the 17.4 and 18.9 μm C_{60} resonances. We did not include the C_{60} PN K3-54 (García-Hernández et al. 2010), because only *Spitzer*/IRS SL and LL spectra are available.

To reduce the *Spitzer*/IRS data, we used the reduction package SMART v.8.2.5 provided by the IRS Team at Cornell University (Higdon et al. 2004) and IRSCLEAN provided by the *Spitzer* Science Center. With IRSCLEAN, we removed the bad pixels. For the SH and LH spectra, we subtracted the sky background using off-set spectra taken in the same program as the on-source spectra, if available. We scaled the flux density of the SL spectra up to, and the LH spectra down to, the SH spectra using the overlapping wavelength regions. Finally, we scaled the flux density of these combined spectra to the Wide-field Infrared Survey Explorer (*WISE*) band 4 photometric value ($\lambda_c=22 \mu\text{m}$), except for IC2501. The flux density at the *WISE* band 4 and the adopting scaling factor matching this band for each object are listed in Table 2.

For IC2501, we estimated the light loss using the Two Micron All-Sky Survey (2MASS) *Ks* band image. By measuring the pixel values of the entire nebula and those inside the area of the SH slit, we estimated that $\sim 39.7\%$ of the light from IC2501 was included

Table 1. *Spitzer*, *ISO*, and *AKARI* observing log.

Nebula	PN G ll.l±bb.b	Spitzer/ISO				AKARI			
		AOR Key/ TDT	Obs. Date yy-mm-dd	PI	SNR	OBSID	Obs. Date yy-mm-dd	PI	SNR
Hen2-68	294.9–04.3	25852417	09-04-03	L. Stanghellini	138	3460047	09-01-26	T. Onaka	26
IC418	215.2–24.2	4909568	04-10-01	D. Cruikshank	105	Saturated			
		82901301 ^a	98-02-22	D. Beintema	87				
		86801205 ^b	98-04-01	M. Barlow	24				
IC2501	281.0–05.6	4905728	04-05-13	D. Cruikshank	747	1740559	08-07-01	Y. Nakada	54
K3-62	095.2+00.7	25847808	08-08-06	L. Stanghellini	208	3460033	08-12-18	T. Onaka	17
M1-6	211.2–03.5	21953024	08-12-07	J. Bernard-Salas	318	3460036	09-03-29	T. Onaka	44
M1-9	212.0+04.3	2194560	08-04-27	J. Bernard-Salas	83				
M1-11	232.8–04.7	19903232	06-11-09	H. Dinnerstein	211	3460037	09-04-11	T. Onaka	52
M1-12	235.3–03.9	25849856	08-11-30	L. Stanghellini	138	3460038	09-04-15	T. Onaka	39
M1-20	006.1+08.3	11315712	05-04-19	M. Bobrowsky	38				
SaSt2-3	232.0+05.7	21958144	08-04-29	J. Bernard-Salas	16				
Tc1	345.2–08.8	11321600	05-03-21	M. Bobrowsky	57				

^aSWS mode^bLWS mode

in the SH entrance of *Spitzer*. Thus, we scaled the flux density of the spectrum by a factor of 2.519.

For IC418, we scaled the flux density of the *Spitzer* SH spectrum up to match that of *ISO*. The spectral resolution of the *ISO* spectrum was reduced to ~600 to match that of *Spitzer*/SH by the Gaussian convolution method. Then, we combined this into a single 2.5–170 μm spectrum. Finally, we scaled the flux density of this spectrum to the *WISE* band 4 photometry with a scaling factor of 1.203 (See Table 2). In the 10–20 μm wavelength range we adopted the *Spitzer*/IRS data, and outside this range we used the *ISO* spectrum.

2.2 AKARI/IRC spectra

Checking for the presence of the 3.3 μm PAH feature is necessary to estimate the extent by which the 8.5 μm C₆₀ band is contaminated by the 8.6 μm PAH feature. Using the intensity ratio of 3.3 μm to 11.3 μm PAH bands, we can estimate the number of C atoms of each PAH grain.

To that end, we analyzed the 2.5–5.5 μm spectra of Hen2-68, IC2501, K3-62, M1-6, M1-11 and M1-12 taken with the Infrared Camera spectrograph (IRC; Onaka et al. 2007) on board of the *AKARI* satellite (Murakami et al. 2007). The data were obtained as part of two different mission programs, AGBGA (IC2501, PI: Y. Nakada) and PNSPEC (the remainder, PI: T. Onaka). The 1'×1' observing window is large enough to include the optical nebulae of these PNe as demonstrated in Section 2.3, therefore, we assume that the loss of the light is negligibly small and we did not perform any correction in flux density. For the data reduction, we used the IRC Spectroscopy Toolkit for the Phase 3 data version.

2.3 Optical and mid-infrared images of C₆₀-containing PNe

To check the apparent size of the nebulae, the nebular shape, and the slit-position in the *Spitzer* observations, we analyzed the archival optical and mid-infrared images from *HST*, Gemini 8.2-m, and ESO/NTT 3.6-m telescopes. These images are necessary to set the outer radii of each PN in *CLOUDY* photo-ionization models (See Section 3).

We downloaded the archival data of IC2501 and K3-62 from the Canadian Astronomy Data Centre (CADC) taken by the Gem-

ini telescopes with the mid-infrared imager and spectrograph T-ReCS for IC2501 and Michelle for K3-62. These data were taken through the observing programs GS-2004B-DD-8 (PI: K.Volk) for IC2501 and GN-2005A-C-4 (PI: S.Kwok) for K3-62. Both images were taken using the Si-5 filter ($\lambda_c=11.6 \mu\text{m}$). We reduced the data of IC2501 and K3-62 using NOAO/IRAF⁶ in a standard manner. The archival *HST* data of Hen2-68 (WFC3/F507N), IC418, M1-6, M1-11, M1-12, and M1-20 (all WFPC2/F656N) were also downloaded from the CADC and reduced using the standard pipeline with STSDAS/MultiDrizzle to obtain higher resolution images. The NTT/EFOSC data of Tc1 taken through the program 64.H-0557(A) (PI: T.Rauch) were downloaded from the ESO archive center, and we reduced the *R*-band image using IRAF. The instrumental distortion was corrected with the XYXYMATCH, GEOMAP, and GEOTRAN IRAF routines, and we aligned the positions of stars in the detector.

The reduced images are presented in Fig. 1. Since our attention is mainly towards the regions where the 17.4 and 18.9 μm C₆₀ bands are detected, we also present the slit position and its size for the *Spitzer*/IRS SH module (slit dimension: 4.7''×11.3''), indicated by the green boxes for IC418, IC2501, and Tc1. For the other PNe which do not show the green boxes, the slit size is larger than the apparent size of the nebulae, and thus, the SH measurements have collected all the light emitted by the nebulae. We do not show the images of M1-9 and SaSt2-3, because there are no high-resolution images available. We were able to measure the nebular size of these two objects using the 2MASS *J*-band images which show that M1-9 and SaSt2-3 have round shaped nebulae with ~4'' and ~2'' radii, respectively.

There are no common characteristics in the morphology of the nebula shape. The C₆₀-containing PNe show different nebular shapes; ring (K3-62), round (Hen2-68, IC2501, Tc1), elliptical (IC418, M1-12, M1-20), bipolar (M1-6), and multi-polar (M1-12). Moreover, blobs are seen in Hen2-68 (~1'' SE from the center of the nebula), in IC2501 (~2'' NW and SE), and in Tc1 (~5'' SE).

⁶ IRAF is distributed by the National Optical Astronomy Observatories, which are operated by the Association of Universities for Research in Astronomy (AURA), Inc., under a cooperative agreement with the National Science Foundation.

We confirm that Tc1 has a faint optical nebula which extends up to $\sim 25''$ (not presented here; See Fig. 6b of Williams et al. 2008).

The Si-5 narrow band images of IC2501 and K3-62 cover the wavelength from ~ 10.8 to $\sim 12.5 \mu\text{m}$. Both PNe show the broad $11 \mu\text{m}$ feature in their *Spitzer*/IRS spectra, as we present below. The carrier of this broad dust feature in IC2501 exists in the nebula as blobs, while that in K3-62 is smoothly distributed and its density peak is $\sim 0.8''$ far away from the central star.

3 PROPERTIES OF THE CENTRAL STARS AND THE NEBULAE

Before studying the IR spectra of our sample, we infer the overall physical properties of the central stars as well as the nebular conditions.

To derive physical parameters of the central stars and the nebulae, we run photo-ionization models for each PN except for Hen2-68, K3-62, IC418, and M1-11 using CLOUDY (Ferland et al. 1998). We refer to the results by Morisset & Georgiev (2009) for IC418 and Otsuka et al. (2013) for M1-11. Since there is no information on gas emission line fluxes, except for $H\beta$, the effective temperature T_{eff} , and the distance d , we could not model Hen2-68 and K3-62 using CLOUDY. The effective temperatures (T_{eff}) of Hen2-68 and K3-62 are from Preite-Martinez et al. (1989) and Kondratyeva (2003), respectively. These models allow us to estimate the contribution from [Ar II] $6.99 \mu\text{m}$ line to the $7.0 \mu\text{m}$ C_{60} band.

3.1 CLOUDY modeling approach

In the CLOUDY calculations, we used Tlusty's non-LTE theoretical atmosphere models for O stars (Hubeny & Lanz 1995). The surface gravities $\log g$ of hot white dwarfs ($T_{\text{eff}} \gtrsim 50\,000$ K) are sometimes $\gtrsim 6$. If our sample contains such hot white dwarfs, they should have highly ionized nebulae showing high ionization potential lines such as He II lines and [O IV] $25.9 \mu\text{m}$. However, our sample does not show such lines in the nebulae. Since the absorption line analysis of the central star of IC418 shows that the $\log g \sim 4$ (Morisset & Georgiev 2009; Patriarchi et al. 1989), we assume that the $\log g$ of other objects in our sample are in the range between ~ 3 and ~ 5 . We used a series of theoretical atmosphere models with T_{eff} in the range from $27\,500$ to $55\,000$ K and the $\log g$ in the range from 3.0 to 4.75 to describe the SED of the central star. We referred to Zhang & Kwok (1993) for the $\log g$ of M1-6, M1-9, M1-12, M1-20, and Tc1 as the first estimate. For SaSt2-3, we used the same $\log g$ as for Tc1.

We adopted a constant hydrogen (H) density for all PNe. We fixed the outer radius at the values measured using the images shown in Fig. 1 and varied the inner radius with the H density to match the observed de-reddened $H\beta$ flux of the whole nebula measured by Dopita & Hua (1997) for SaSt2-3 and Cahn et al. (1992) for the others. The distances to each PN estimated by Tajitsu & Tamura (1998) are adopted, except for SaSt2-3. For this source, we adopted the upper value of Pereira & Miranda (2007), namely 6 kpc.

For the gas-phase elemental abundances X/H, we adopted the observed values by prior works as a first guess and varied these to match the observed flux densities of over 30 emission lines of He/C/N/O/Ne/S/Cl/Ar in UV to mid-IR wavelength, except for SaSt2-3 (14 lines). We adopted the line-ratios measured by Sharpee et al. (2007) for IC2501 and Henry et al. (2010) for M1-6, M1-9, and M1-12, by Wang & Liu (2007) for

M1-20, Pereira & Miranda (2007) for SaSt2-3, and compiled by Pottasch et al. (2011) for Tc1. The emission-line fluxes in the mid-IR wavelength range were measured by us for all objects in our sample. We did not include the [Ar II] $6.99 \mu\text{m}$ as an Ar abundance constraint.

Thus, we considered line fluxes from He I, C II, C III], [N II], [O I,II,III], [Ne II,III], [S II,III,IV], [Cl III], and [Ar III,IV].

There are no UV spectra of M1-6, M1-9, M1-12, M1-20, and SaSt2-3 required to determine the C abundances using collisionally excited lines such as C III] $1906/09 \text{ \AA}$. For the C abundances of these PNe we set the value according to

$$[C/Ar] = -0.89 \times [Ar/H] + 0.49, \quad (1)$$

which is established among 115 Milky Way PNe and the C abundances are estimated using collisionally excited C emission lines in the UV wavelength (Otsuka in preparation). We updated collisional strengths and transition probabilities of C III], [O II,III], [N II], [Ne II,III,IV], [S II,III], [Cl II,III], and [Ar II,III,IV] lines, which are the same data listed in Table 7 of Otsuka et al. (2010). Reliable dielectric recombination (DR) rate measurements do not exist for low stages of ionization of S at photo-ionization temperatures (CLOUDY manual), thus we adopted the scaled DR rate of oxygen for the sulfur line calculations, to match the observed [S II].

3.2 Results of the CLOUDY modeling and comparison with non C_{60} -containing PNe

The results of the best model fits are listed in Table 3. The second to fourth columns show the effective temperatures, the luminosities L_* of the central stars, and surface gravities, respectively. The uncertainties in the T_{eff} and $\log g$ are within 1000 K and 0.2 cm s^{-2} , respectively. Since the distances to each PN have a large uncertainty, typically a factor of ~ 1.5 - 2 , the uncertainty in $\log(L_*/L_\odot)$ is ~ 0.35 - 0.6 . The fifth column is the type of the central star, from Weidmann & Gamen (2011a,b). The predicted $F([\text{Ar II}] 6.99 \mu\text{m})/F([\text{Ar III}] 8.99 \mu\text{m})$ ratios, which are used in the $7.0 \mu\text{m}$ C_{60} flux measurements (See Section 4.4 and Appendix), are listed in the last column.

The gas abundances derived by the models are in the eighth column. The uncertainties in the derived gas abundances are within 0.1 dex. The difference between the observed and our model predicted gas abundances is within 0.1 - 0.2 dex. All objects are C-rich (i.e., the C/O ratio > 1) and the elemental composition is very similar within the sample, suggesting that these PNe have evolved from similar progenitor stars. As we mentioned above, the C abundances in M1-6, M1-9, M1-12, and M1-20, and SaSt2-3 are not determined using collisionally excited C lines yet. In order to accurately measure the C/O ratio, we need to detect collisionally excited C lines or C and O recombination lines in these C_{60} -containing PNe, in the future. The average Ar abundance, which indicates the initial metallicity of the progenitors, among 9 of the objects in our sample is 5.99 (Ar=6.55; Lodders 2003), corresponding to the metallicity of $Z \sim 0.005$ in Ar ($0.27 Z_\odot$), which is close to the typical metallicity of the Small Magellanic Cloud. Plotting the estimated L_* and T_{eff} on the He-burning tracks from Vassiliadis & Wood (1994) with $Z=0.004$ shows that the initial mass of the objects is ~ 1.5 - $2.5 M_\odot$. The chemical abundances of our C_{60} -containing PNe can be explained by the AGB nucleosynthesis models for the initially 1.5 - $2.5 M_\odot$ stars with $Z=0.004$ by Karakas (2010) (Table 4).

In the last line of Table 4, we list the average abundances of non C_{60} -containing Galactic C-rich PNe taken from Pottasch & Bernard-Salas (2006). The abundances of C_{60} PNe are

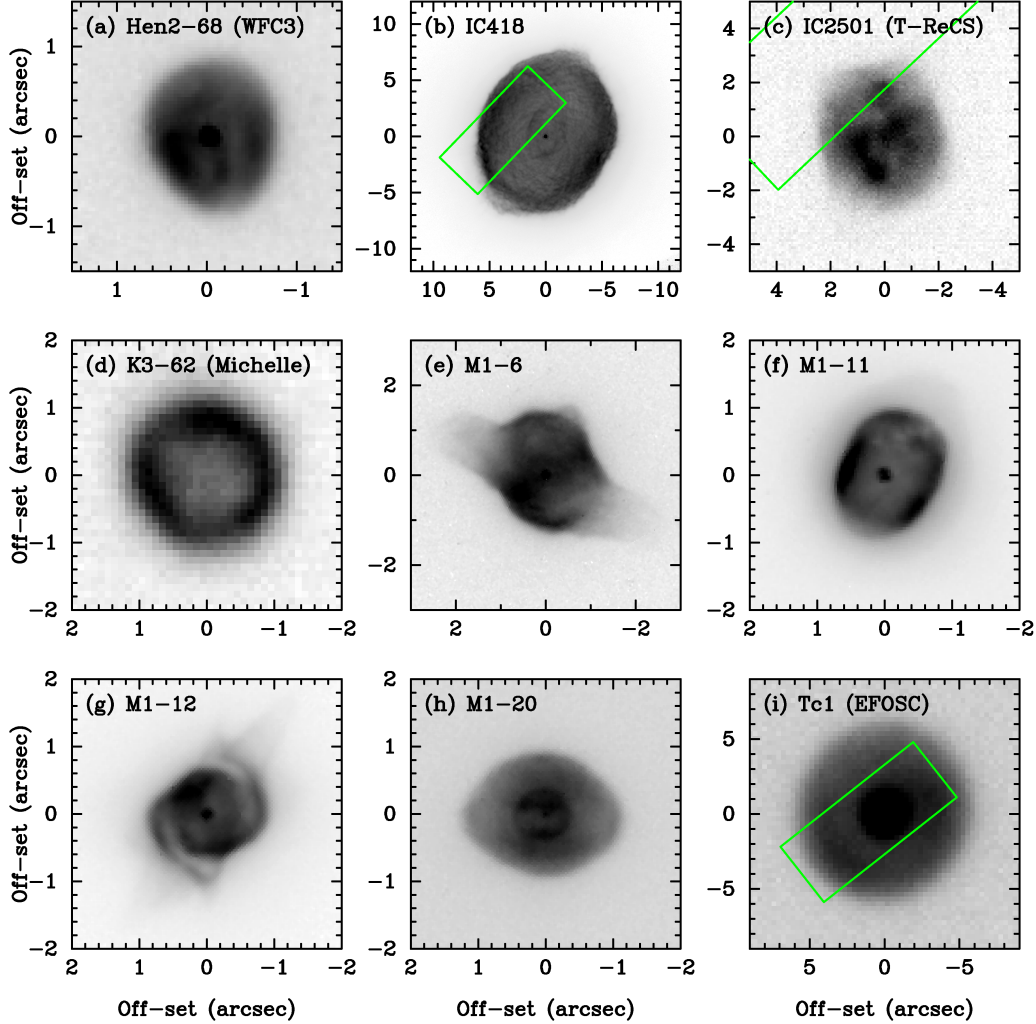


Figure 1. Imaging of the objects in our sample. North is up and east is left. In IC418, IC2501, and Tc1, the position and the size of *Spitzer*/IRS SH slit are indicated by the green boxes. The slit size of the SH module is larger than the apparent size for the other PNe.

Table 3. Properties of the central stars and the nebulae derived photo-ionization models.

Nebula	T_{eff} (K)	$\log(L_*/L_{\odot})$	$\log g$ (cm s^{-2})	Type of central star	P-Cygni	d (kpc)	C/N/O/Ne/S/Ar ($\text{Log } X/H+12$)	$F([\text{Ar II}] 6.99 \mu\text{m})/$ $F([\text{Ar III}] 8.99 \mu\text{m})$
Hen2-68	40 800	?	?	?	?	4.90	?	0.65
IC418	36 700	3.88	3.55	H-rich	y	1.26	8.90/8.00/8.60/8.00/6.65/6.20	1.0
IC2501	51 650	3.17	4.75	wels?	y	2.20	8.77/7.88/8.58/7.94/6.56/6.13	0.03
K3-62	45 000	?	?	?	?	6.00	?	0.09
M1-6	34 960	3.31	3.50	[WC10-11]	?	4.10	8.76/7.91/8.60/8.05/6.49/5.95	0.18
M1-9	43 500	3.41	4.50	?	?	9.0	8.81/7.69/8.34/7.68/6.25/5.89	0.04
M1-11	31 830	3.67	3.30	[WC10-11]	?	2.10	8.49/7.89/8.30/7.67/6.15/5.95	5.20
M1-12	31 660	3.54	3.40	[WC10-11]	?	3.90	8.74/7.75/8.50/7.80/6.48/5.81	1.99
M1-20	45 880	3.59	4.75	wels	?	7.30	8.70/7.85/8.58/7.85/6.76/5.94	0.02
SaSt2-3	29 750	2.80	3.30	OB.	?	6.00	8.72/7.49/8.23/7.68/6.17/5.93	4.71
Tc1	34 060	3.40	3.30	Of(H)	y	3.00	8.71/7.83/8.61/7.98/6.58/6.07	0.10

not very different from those of these non C_{60} -containing PNe, except for N. This might be due to the two α capturing by ^{14}N , because the Ne abundances in C_{60} -containing PNe are slightly larger than the model predictions. The low Ar abundance in C_{60} -containing PNe (5.81-6.20) suggests that the progenitors are an older population.

3.3 Presence of the stellar wind

We checked the presence of P-Cygni profiles in the $\text{Ly}\alpha$ 1215 Å line in the archived Far Ultraviolet Spectroscopic Explorer (*FUSE*) and International Ultraviolet Explorer (*IUE*) spectra, as listed in the sixth column. We found that IC418, IC2501, and Tc1 indeed show the P-Cygni profile. There are no data for Hen2-68, K3-62,

Table 4. Comparison of the predicted abundances for different initial mass stars with $Z=0.004$ by Karakas (2010) and the observed abundances.

initial mass	C	N	O	Ne	S
1.50 M_{\odot}	8.46	7.65	8.23	7.42	6.70
1.75 M_{\odot}	8.80	7.70	8.25	7.51	6.70
1.90 M_{\odot}	8.94	7.71	8.25	7.61	6.70
2.10 M_{\odot}	9.00	7.68	8.25	7.67	6.70
2.25 M_{\odot}	9.26	7.72	8.27	8.00	6.72
2.50 M_{\odot}	9.38	7.76	8.27	8.20	6.73
C_{60} PNe	8.49-8.90	7.49-8.00	8.23-8.61	7.67-8.05	6.15-6.76
non- C_{60}	8.85	8.23	8.56	8.06	6.85
C-rich PNe ^a					

^aThe averaged value between 11 C-rich Galactic PNe listed in Table A1 of Pottasch & Bernard-Salas (2006). The averaged Ar abundance is 6.42.

SaSt2-3, M1-6 and M1-12 and no data for M1-11 with enough SNR to check for the presence of a P-Cygni $Ly\alpha$ profile. However, since M1-6, M1-11, M1-12, and M1-20 have Wolf-Rayet like central stars ([WC10,11]; weak emission line stars, *wels*), which show the broad C III,IV lines, there has to be a strong wind (e.g., Acker & Neiner 2003).

4 THE IR SPECTRA OF GALACTIC C_{60} PNE

4.1 Overview: Spectral Features and Variations in 5-36 μm

The 5.3-35 μm spectra are presented in Fig. 2. The data of M1-11 shortwards of 10 μm are from ESO VLT/VISIR (See Otsuka et al. 2013). The positions of the C_{60} bands and several atomic lines seen in the spectra are indicated by the dotted lines. The blue edge of the SH spectrum of SaSt2-3 is very noisy ($\text{SNR} \lesssim 5$). Therefore, we combined the 5.3-14 μm SL, >13.5 μm SH, and LH data into a single spectrum. In the range between 5.3 and 23 μm , we fitted the underlying feature-less continuum by a third to fifth order single spline function indicated by the green lines. Since there is no spectral data between 5-7 μm for M1-11 and <10 μm for IC2501, we used the *AKARI*/IRC 2.5-5.0 μm spectra as anchor data at the shortest wavelength. We subtracted the spline component from the data before measuring the fluxes of the C_{60} lines. The details of the *AKARI*/IRC 2.5-5.0 μm spectra are discussed in Section 4.5.

There are strong variations in the intensity of the 8.5, 17.4, and 18.9 μm C_{60} bands relative to the local dust continuum indicated by the green lines, with SaSt2-3 and Tc1 showing especially strong 8.5, 17.4, and 18.9 μm C_{60} bands.

The 6-9 μm PAH bands are seen in all PNe, although the band-profiles are different from ones frequently seen in non- C_{60} PNe. There is the possibility that the 6.99 and 7.07 μm C_{70} resonances might contribute to the 7.0 μm band. However, we could not detect any C_{70} bands in our sample, except for the already reported features in Tc1 (Cami et al. 2010). Therefore, in the PNe in our sample except for Tc1, the 7.0 μm line is concluded to be due to a complex of the 6.92 μm aliphatic vibration band, the [Ar II] 6.99 μm , and the 7.0 μm C_{60} band. Except for SaSt2-3 and Tc1, the 8.5 μm C_{60} bands are contaminated by the 8.6 μm PAH band. We focus on the 17.4 and 18.9 μm C_{60} bands and on the 6-9 μm complex in Sections 4.2 and 4.3, respectively.

The broad 11 and 30 μm features are also seen in all PNe. Fig. 3 shows the spectra normalized to the flux density at 20 μm . All the spectra show a thermal dust continuum; the slope (clearly visible over 12-23 μm) is different for the different objects, pointing

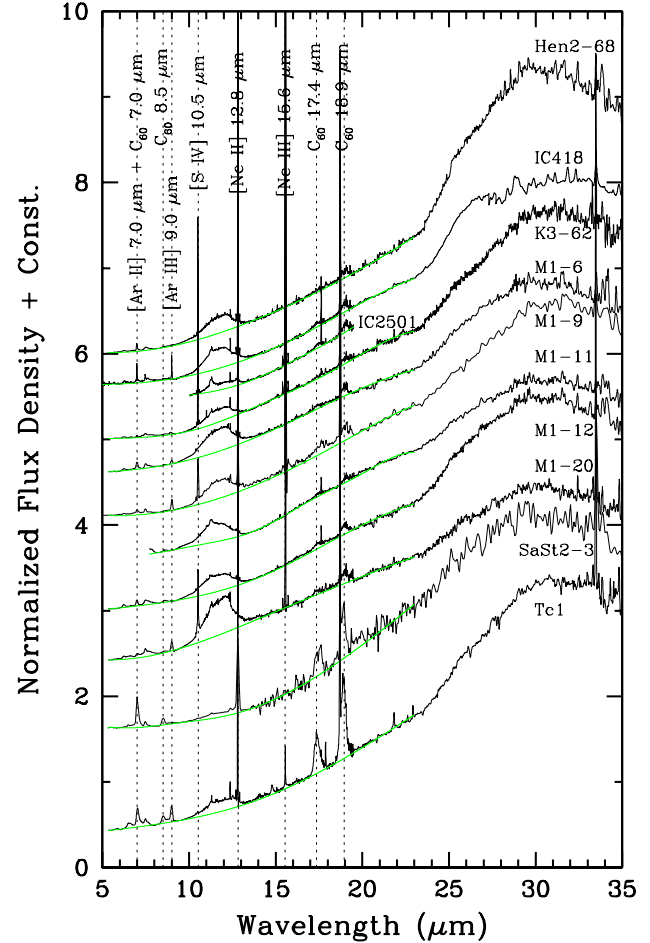


Figure 2. The 5.3-35 μm *Spitzer*/IRS and *ISO* spectra normalized to the flux density at 20 μm . The green lines are base lines determined by fitting the underlying feature-less continuum with third to fifth order spline in the range from 5.3 to 23 μm , except for IC2501 and M1-11. For IC2501 we determined the continuum over 2.5-5.0 μm and 10-19.6 μm , while for M1-11 we used 2.5-5.0 and 8-23 μm . The flux density normalization for IC2501 was using the extrapolated continuum from 10-19.6 μm continuum (the green line). Several emission features seen in these spectra are indicated by dotted lines. The 17.4 and 18.9 μm C_{60} bands are also presented in Fig. 4. The 7.0 and 8.5 μm C_{60} bands and the 6-9 μm PAH bands are also presented in Fig. 5.

to different dust temperatures, caused by the difference in irradiation. The strengths of the 17.4 μm and 18.9 μm C_{60} bands are not changing with the local dust continuum. We investigate correlations between the C_{60} band strength, the broad 11 μm band, and the local dust continuum in the following sections.

4.2 The 17.4 and 18.9 μm C_{60} line profiles

Fig. 4 displays the continuum subtracted spectra over 16.5-20.1 μm , showing the 17.4 and 18.9 μm C_{60} features in all objects in our sample. Narrow emission lines are also seen in the same range; e.g., H γ 17.61 μm ($n=11-18$), [P III] 17.89 μm ($^2P_{1/2}-^2P_{3/2}$), [S III] 18.71 μm ($^3P_{1/2}-^3P_{2/2}$), and H δ 19.06 μm ($n=7-8$), as well as spike noise. Since the red-wings of the 18.9 μm C_{60} bands in M1-11 and M1-20 are noisy, the full width at zero intensity of the 18.9 μm C_{60} band is a little bit larger than that in the others. The narrower width

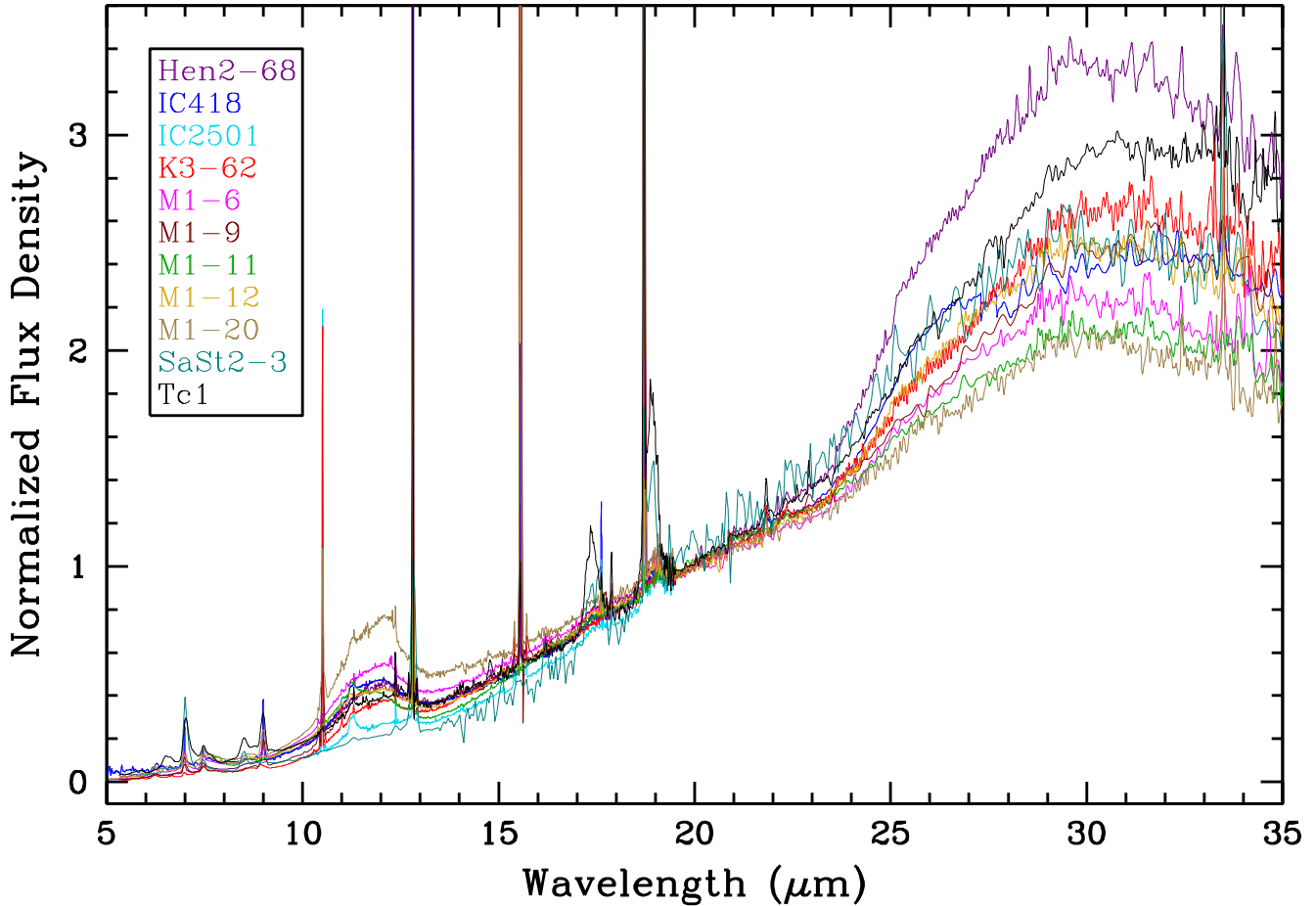


Figure 3. The *Spitzer*/IRS and *ISO* spectra normalized to the flux density at 20 μm .

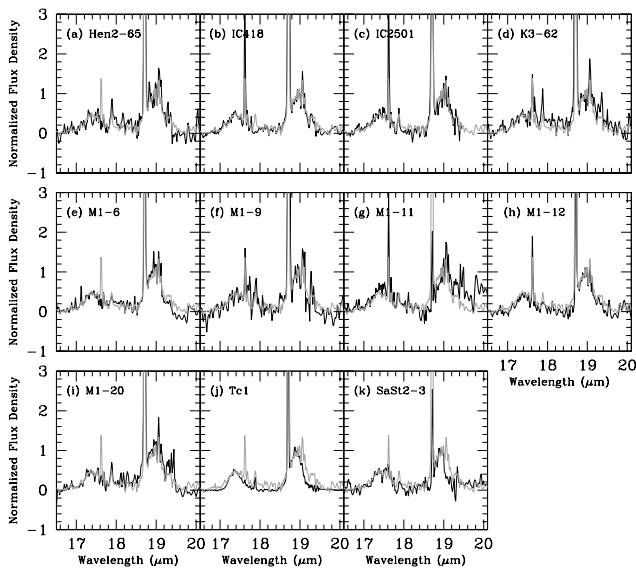


Figure 4. The local continuum subtracted spectra over 16.5-20.1 μm , normalized to the peak flux density in the 18.9 μm C_{60} band. The gray lines represent the observed spectra of each object and the grey lines show the average spectrum among all objects.

of the 18.9 μm C_{60} band in SaSt2-3 relative to the other objects is due to the low SNR around 19 μm .

Although there are some issues in the data quality as explained above, the normalized line profiles of the 17.4 and 18.9 μm C_{60} bands are almost similar to each other, as can be seen from the average spectrum, which is plotted in grey in each panel.

4.3 The 7.0 and 8.5 μm C_{60} and the broad 6-9 μm complex

We investigate the 6-9.2 μm continuum-subtracted spectra (Fig. 2), and the result is shown in the upper panel of Fig. 5. As a reference, we show the 6-9.2 μm line profile of the C-rich young PN NGC7027 in the lower panel of Fig. 5. We did not detect C_{60} bands in this PN. According to the classification of 6-9 μm PAH profiles by Peeters et al. (2002), NGC7027 is a class B PN. Bernard-Salas et al. (2009) classified the 6-9 μm PAH profiles of 11 Magellanic Cloud PNe with no C_{60} as class B among 14 objects. Hence a comparison between our sources and NGC7027 is useful to investigate the differences between C_{60} and non- C_{60} PNe and also to see the contribution from the 6.92 μm aliphatic emission and from the 8.6 μm PAH emission to the 7.0 μm and 8.5 μm C_{60} bands, respectively.

The line-profiles in the C_{60} -containing PNe are similar to each other, except for the 6.2 and 8.5 μm bands. Only two sources, Tc1 and SaSt2-3 clearly show the strong 8.5 μm C_{60} band, while the 6.2 μm PAH band is very weak. In other sources these bands are heavily

Table 5. 3.3, 6.2, 8.6, and 11.3 μm PAH band fluxes.

Nebula	λ_{obs} (μm)	$F(\text{PAH } 3.3)$ ($\text{erg s}^{-1} \text{cm}^{-2}$)	λ_{obs} (μm)	$F(\text{PAH } 6.2)$ ($\text{erg s}^{-1} \text{cm}^{-2}$)	λ_{obs} (μm)	$F(\text{PAH } 8.6)$ ($\text{erg s}^{-1} \text{cm}^{-2}$)	λ_{obs} (μm)	$F(\text{PAH } 11.3)$ ($\text{erg s}^{-1} \text{cm}^{-2}$)	$F(3.3)/$ $F(11.3)$
Hen2-68	3.30	1.38(-13) \pm 4.83(-14)	6.23	5.74(-13) \pm 1.04(-14)	8.70	2.09(-13) \pm 4.68(-15)	11.26	2.02(-13) \pm 3.39(-14)	0.68 \pm 0.12
IC418	3.29	1.96(-11) \pm 1.11(-12)	6.27	3.46(-11) \pm 2.03(-13)	8.68	1.62(-11) \pm 5.45(-14)	11.26	2.74(-11) \pm 8.62(-13)	0.72 \pm 0.23
IC2501	3.30	3.18(-12) \pm 1.16(-13)					11.28	5.94(-12) \pm 3.74(-13)	0.54 \pm 0.04
K3-62	3.30	2.86(-13) \pm 3.46(-14)	6.23	1.41(-12) \pm 2.99(-14)	8.72	7.38(-13) \pm 5.96(-15)	11.25	8.94(-13) \pm 6.03(-14)	0.32 \pm 0.04
M1-6	3.30	4.05(-13) \pm 4.02(-14)	6.23	2.58(-12) \pm 3.33(-14)	8.66	5.50(-13) \pm 8.25(-14)	11.27	5.81(-13) \pm 8.75(-14)	0.70 \pm 0.13
M1-9			6.23	1.75(-13) \pm 1.56(-15)	8.71	6.28(-14) \pm 1.30(-14)	11.28	1.25(-13) \pm 1.87(-14)	
M1-11	3.29	7.02(-12) \pm 2.89(-13)			8.69	5.79(-12) \pm 2.95(-13)	11.29	1.16(-11) \pm 7.85(-13)	0.61 \pm 0.04
M1-12	3.29	5.41(-13) \pm 3.96(-14)	6.22	3.26(-13) \pm 7.04(-14)	8.69	8.60(-13) \pm 1.24(-13)	11.25	8.61(-13) \pm 1.23(-13)	0.63 \pm 0.10
M1-20			6.22	7.68(-13) \pm 2.23(-14)	8.71	3.98(-13) \pm 8.54(-14)	11.26	8.56(-13) \pm 1.63(-13)	
SaSt2-3			6.25	1.49(-14) \pm 9.90(-16)			11.29	1.36(-14) \pm 4.68(-16)	
Tc1			6.20	8.08(-13) \pm 5.42(-14)			11.27	1.40(-12) \pm 2.20(-13)	

contaminated by PAHs at 8.6 and 6.2 μm , respectively (see Fig. 5a), thus hampering the flux measurements of the 7.0 and 8.5 μm C_{60} bands. The 7.2-8.1 μm band profile in the C_{60} -containing PNe are quite different from that in NGC7027. While NGC7027 and other class B objects exhibit 7.7 μm emission peaking between 7.8 and 8 μm , our objects show little emission in this wavelength range but instead emit the bulk of their emission shortwards of the 7.8 μm complex. Hence, despite the H I contamination, this suggests that they likely exhibit class A profiles. The carrier of the latter is believed to be more processed than that of the class B profiles (Peeters et al. 2002; Sloan et al. 2005, 2007; Boersma et al. 2008), because the class A and B profiles tend to be observed in reflection nebulae and H II regions and in AGB stars and PNe, respectively.

A 7.30 μm emission band is seen in K3-62. Scott & Duley (1996) and Scott et al. (1997) found that an emission feature at this wavelength may be due to chemically processed hydrogenated amorphous carbons (HAC) grains. HAC is a generic name for a mixture of aliphatic and aromatic carbon, consisting of PAH clusters embedded within a matrix of aliphatically bonded material. Moreover, a 7.49 μm emission band is detected in all PNe. This emission band is possibly due to the 7.50 μm C_{60}^+ resonance. On the other hand, the 7.49 μm feature will have large contamination from the H I 7.46 μm ($n=6-5$) and the H I 7.50 μm ($n=8-6$). In IC418, for example, our measured respective fluxes of H I 7.46 μm and H I 7.50 μm are 1.59(-11) and 5.89(-12) $\text{erg s}^{-1} \text{cm}^{-2}$. The observed intensity ratio of H I 7.46 μm to 7.50 μm (2.70) is smaller than the theoretical value (3.77) in the case of $T_e=10^4$ K and $n_e=10^3 \text{cm}^{-3}$ derived by Storey & Hummer (1995). Therefore, we conclude that the 7.49 μm complex is a combination of both H I and C_{60}^+ . We assume that only part of the 7.49 μm feature is due to H I, and the remainder is carried by C_{60}^+ .

The fluxes of the 6.2 and 8.6 μm PAH bands are listed in Table 5.

4.4 Flux measurements of the C_{60} lines

We employed multiple Gaussian fitting for all C_{60} bands to separate the various components in each feature. The details are discussed in the Appendix and the results are listed in Table 6. We also list the total flux of the 7.0 μm complex composed of the 7.0 μm C_{60} band, the 6.92 μm aliphatic band, and the [Ar II] 6.99 μm line, as well as the total flux of the 8.5 μm C_{60} and 8.6 μm PAH complex. The total fluxes can be treated as upper limits to the C_{60} fluxes. In the fits of the 17.4 μm and 18.9 μm C_{60} bands, we employed two or three component Gaussians.

The measurement errors of the central wavelength, the

Table 7. The flux ratios of the C_{60} lines relative to the 18.9 μm C_{60} band.

Nebula	$F(7.0)/F(18.9)$	$F(8.5)/F(18.9)$	$F(17.4)/F(18.9)$
Hen2-68	1.25 \pm 0.22	0.28 \pm 0.05	0.50 \pm 0.11
IC418	0.74 \pm 0.08	0.50 \pm 0.03	0.46 \pm 0.03
IC2501			0.50 \pm 0.05
K3-62	0.32 \pm 0.05	0.19 \pm 0.02	0.46 \pm 0.06
M1-6	2.46 \pm 0.15	0.26 \pm 0.05	0.48 \pm 0.09
M1-9	0.70 \pm 0.06	0.14 \pm 0.01	0.51 \pm 0.10
M1-11		0.55 \pm 0.11	0.52 \pm 0.14
M1-12	0.98 \pm 0.05	0.51 \pm 0.05	0.45 \pm 0.05
M1-20	0.78 \pm 0.09	0.42 \pm 0.10	0.50 \pm 0.08
SaSt2-3	1.04 \pm 0.11	0.39 \pm 0.07	0.55 \pm 0.13
Tc1	0.77 \pm 0.03	0.29 \pm 0.01	0.49 \pm 0.02

FWHM, and the fluxes of the C_{60} lines are 1- σ . The 17.4 μm and 18.9 μm C_{60} bands in Tc1 include a contribution from C_{70} (Cami et al. 2010), with the flux ratios of the C_{60} to C_{70} at 17.4 and 18.9 μm of 3.44 and 9.29, respectively. For Tc1, we also listed the fluxes of the 17.4 and 18.9 μm C_{60} lines after the contribution from C_{70} lines are subtracted. For SaSt2-3, the fluxes of 17.4 and 18.9 μm C_{60} are also listed when the above ratios for Tc1 are applied, although we could not clearly detect any C_{70} bands in SaSt2-3.

The flux ratios relative to 18.9 μm C_{60} band are summarized in Table 7. In Tc1, the 7.0 μm feature is a complex of the C_{60} and C_{70} , but the exact fraction of each component to the 7.0 μm band is unknown. Therefore, the $F(7.0 \mu\text{m})/F(18.9 \mu\text{m})$ value in Tc 1 represents an upper limit. In other PNe, since we could not detect any C_{70} emissions, the contribution of the C_{70} to the 7.0 μm band is very small. The $F(17.4 \mu\text{m})/F(18.9 \mu\text{m})$ ratio is almost constantly ~ 0.5 in all objects in our sample as we argued in Section 4.2, while there is more scatter in the $F(7.0 \mu\text{m})/F(18.9 \mu\text{m})$ and the $F(8.5 \mu\text{m})/F(18.9 \mu\text{m})$ ratios due to the contributions from the [Ar II] 6.99 μm line and the 8.6 μm PAH band to the 7.0 and 8.5 μm C_{60} bands, respectively.

4.5 The 3.3 μm PAH band in AKARI spectra

The reduced AKARI spectra show emission bands at 3.2-3.6 μm , which are due to aromatic and aliphatic hydrocarbon species. The strong resonance at 3.3 μm is attributed to the aromatic C-H stretching vibration in PAHs and the 3.4-3.6 μm faint broad band is due to aliphatic hydrocarbon. We should note that the 3.3 μm PAH band is always contaminated with the H I 3.2 μm line ($n=5-9$).

Using the theoretical intensity ratio of H I 3.2 μm to 4.65 μm ($n=5-7$) = 0.46 in the case of the electron temperature $T_e=10^4$ K and the electron density $n_e=10^4 \text{cm}^{-3}$ (Storey & Hummer 1995),

Table 6. Results of the Gaussian fits for the C₆₀ lines.

Nebula	λ_{obs} (μm)	FWHM (μm)	Flux ($\text{erg s}^{-1} \text{cm}^{-2}$)	Nebula	λ_{obs} (μm)	FWHM (μm)	Flux ($\text{erg s}^{-1} \text{cm}^{-2}$)
Hen2-68	6.98	5.99(-2) \pm 1.54(-3)	1.06(-12) \pm 4.01(-14) ^a 9.78(-13) \pm 4.28(-14) ^b	M1-11	8.55	1.89(-1) \pm 9.51(-3)	3.82(-12) \pm 3.46(-13) ^c 9.61(-12) \pm 4.55(-13) ^d
	8.51	1.87(-1) \pm 5.66(-3)	2.16(-13) \pm 7.72(-15) ^c 4.25(-13) \pm 9.02(-15) ^d		17.43	3.56(-1) \pm 6.52(-2)	3.60(-12) \pm 7.74(-13)
	17.43	4.17(-1) \pm 1.12(-2)	3.95(-13) \pm 5.03(-14)		19.02	3.96(-1) \pm 5.14(-2)	6.89(-12) \pm 1.16(-12)
	18.96	4.49(-1) \pm 4.90(-2)	7.83(-13) \pm 1.34(-13)		M1-12	6.99	1.13(-1) \pm 1.80(-3)
IC418	7.01	1.95(-1) \pm 1.01(-2)	8.62(-11) \pm 2.74(-12) ^a 3.28(-11) \pm 3.07(-12) ^b	8.55		2.18(-1) \pm 1.03(-2)	1.24(-12) \pm 9.58(-14) ^c 2.10(-12) \pm 1.02(-13) ^d
	8.51	1.45(-1) \pm 1.37(-2)	5.75(-12) \pm 6.67(-13) ^c 2.20(-11) \pm 8.61(-13) ^d	17.40		3.59(-1) \pm 2.14(-2)	1.09(-12) \pm 1.09(-13)
	17.38	3.48(-1) \pm 1.12(-2)	2.04(-11) \pm 7.93(-13)	18.94		4.02(-1) \pm 1.63(-2)	2.41(-12) \pm 1.20(-13)
	18.93	4.34(-1) \pm 1.86(-2)	4.44(-11) \pm 2.04(-12)	M1-20	7.02	1.57(-1) \pm 2.60(-3)	7.91(-13) \pm 2.37(-14) ^a 6.83(-13) \pm 1.32(-14) ^b
IC2501	17.44	3.49(-1) \pm 2.53(-2)	1.97(-12) \pm 1.93(-13)		8.53	2.29(-1) \pm 3.73(-2)	3.67(-13) \pm 8.21(-14) ^c 6.45(-13) \pm 1.43(-13) ^d
	19.02	3.78(-1) \pm 4.82(-2)	3.93(-12) \pm 6.08(-13)		17.38	3.71(-1) \pm 3.88(-2)	4.36(-13) \pm 5.39(-14)
	K3-62	6.99	7.94(-2) \pm 1.33(-3)		6.05(-13) \pm 1.77(-14) ^a 4.20(-13) \pm 3.74(-14) ^b	18.98	3.58(-1) \pm 2.80(-2)
8.56		1.26(-1) \pm 4.43(-3)	2.46(-13) \pm 1.12(-14) ^c 9.83(-13) \pm 1.27(-14) ^d	SaSt2-3	7.01	1.23(-1) \pm 2.16(-3)	4.52(-13) \pm 1.28(-14) ^a 3.15(-13) \pm 1.98(-14) ^b
17.35		3.25(-1) \pm 6.29(-2)	6.04(-13) \pm 1.25(-14)		8.50	1.71(-1) \pm 9.00(-4)	1.19(-13) \pm 7.77(-16)
18.99		4.43(-1) \pm 4.79(-2)	1.32(-12) \pm 1.66(-13)		17.39	3.11(-1) \pm 5.80(-2)	1.68(-13) \pm 3.55(-14)
M1-6	6.99	1.34(-1) \pm 2.04(-3)	5.50(-12) \pm 1.40(-14) ^a 4.88(-12) \pm 1.51(-13) ^b	Tc1	18.92	2.92(-1) \pm 1.77(-2)	1.30(-13) \pm 2.75(-14) ^e 3.03(-13) \pm 2.40(-14)
	8.51	1.74(-1) \pm 2.08(-3)	5.09(-13) \pm 9.18(-14) ^c 1.06(-12) \pm 1.24(-13) ^d		7.03	1.66(-1) \pm 4.44(-3)	2.74(-13) \pm 2.17(-14) ^e 1.75(-11) \pm 5.70(-13) ^a 1.67(-11) \pm 5.86(-13) ^b
	17.36	3.91(-1) \pm 5.67(-2)	9.45(-13) \pm 1.66(-13)		8.50	1.90(-1) \pm 3.00(-3)	6.22(-12) \pm 1.34(-14)
	18.90	3.56(-1) \pm 1.62(-2)	1.98(-12) \pm 1.07(-13)		17.38	3.66(-1) \pm 1.08(-2)	1.38(-11) \pm 5.00(-13) ^e 1.07(-11) \pm 3.87(-13) ^e
M1-9	7.00	1.36(-1) \pm 2.95(-3)	3.47(-13) \pm 8.16(-15) ^a 2.94(-13) \pm 8.62(-15) ^b		18.90	3.47(-1) \pm 4.39(-3)	2.40(-11) \pm 4.42(-13) ^e 2.17(-11) \pm 3.99(-13) ^e
	8.54	2.03(-1) \pm 8.70(-3)	5.93(-14) \pm 2.79(-15) ^c 1.22(-13) \pm 1.33(-14) ^d				
	17.40	3.53(-1) \pm 5.23(-2)	2.15(-13) \pm 3.77(-14)				
	18.89	3.73(-1) \pm 2.19(-2)	4.19(-13) \pm 3.32(-14)				

^aTotal flux of the 7.0 μm line.

^bThe residual flux after the predicted [Ar II] 6.99 μm flux and 6.92 μm aliphatic band feature are subtracted. The value is the flux of the C₆₀ 7.0 μm feature.

^cThe flux of C₆₀ 8.5 μm feature measured using a two-component Gaussian fit. For SaSt2-3 and Tc1, a single Gaussian is fitted to the C₆₀ 8.5 μm feature.

^dTotal flux of the C₆₀ 8.5 μm and PAH 8.6 μm bands.

^eby applying the flux ratio of C₆₀/C₇₀ observed in Tc1 by Cami et al. (2010).

we removed the contribution of the H I 3.2 μm line from the 3.3 μm emission band, assuming that the full width at half maximum (FWHM) velocities of H I 3.2 and 4.65 μm are the same and the line-profile of these H I lines can be represented by a single Gaussian. The resulting spectra in the range from 3.1 to 3.9 μm are presented in Fig. 6. In panels a-h, as a comparison, we also present the ISO/SWS spectrum of NGC7027 indicated by grey lines. The spectral resolution of NGC7027 data was reduced down to \sim 110 at 3.3 μm using Gaussian convolution to match that of AKARI/IRC. For the purpose of removing the H I 3.2 μm , we used the H I 4.65 μm instead of H I 3.73 μm , because the SNR of local continuum around 4.65 μm is better (IC418, in particular) and there is less contribution from nearby emission-lines. The positions of some aliphatic hydrocarbons seen in M1-6 and NGC7027 are indicated by the dotted lines (a). The flux density is normalized to the peak intensity of the 3.3 μm PAH band and the local continuum of these spectra is subtracted. Due to low SNR of Hen2-68 and K3-62, we overestimated the flux of H I 4.65 μm in both PNe, and we overcorrected the component from H I 3.2 μm . The central wavelength and the fluxes of the solo 3.3 μm PAH band error are listed in the second and third columns of Table 5.

For IC418, we confirmed the presence of the broad PAH 3.3 μm emission band in the ISO spectrum. The spectral resolution was

also reduced to 110 at 3.3 μm using Gaussian convolution to match that of AKARI/IRC. We again removed the contribution of the H I 3.2 μm line by employing the same technique as described above and we again measured the solo flux of the 3.3 μm PAH band. The resultant spectrum and the result of the flux measurement are also shown in Fig. 6 and Table 5, respectively.

The 3.2-3.6 μm band profile is very similar amongst the sources in our sample. All our sources exhibit the 3.3 μm PAH band.

4.6 The size of PAHs

The 3.3/11.2 μm PAH band ratio depends on the hardness of the radiation field (i.e. the average photon energy that is absorbed) and the PAH size distribution since 1) the intrinsic PAH flux ratio $F(3.3 \mu\text{m})/F(11.3 \mu\text{m})$ decreases with increasing number of the C-atoms and 2) the 3.3 μm PAH arises mainly from PAHs containing between roughly 30 and 70 C atoms while the 11.2 μm PAH is dominated by PAHs containing between about 80 to several hundred carbon atoms (Ricca et al. 2012; Draine & Li 2007; Schutte et al. 1993; Allamandola et al. 1989). The observed $F(3.3 \mu\text{m})/F(11.3 \mu\text{m})$ ratios are given in the last column of Table 5. The average $F(3.3 \mu\text{m})/F(11.3 \mu\text{m})$ is 0.60 among our sample. We also mea-

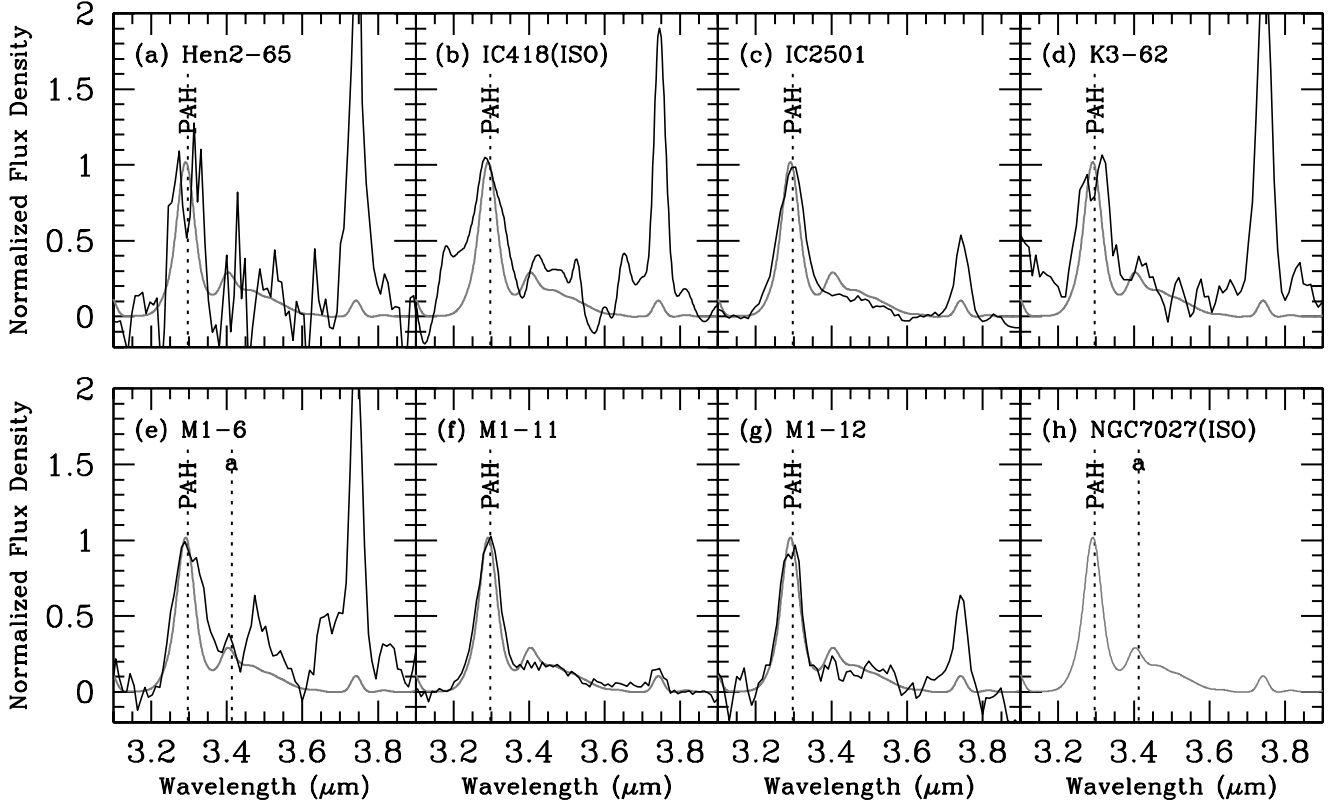


Figure 6. The *AKARI/IRC* and *ISO* 3.1–3.9 μm spectra. We removed the H I 3.2 μm line. The grey lines are the *ISO/SWS* spectrum of the C-rich PN NGC7027. The 3.4–3.6 μm faint broad band is due to aliphatic hydrocarbon. The emission around 3.7 μm is the H I 3.73 μm ($n=5-8$). The dashed lines marked with “a” in M1-6 and NGC7027 represent the 3.38/3.40 μm aliphatic asymmetric CH_3 , CH_2 stretch.

Table 8. The 3.3 and 11.3 μm PAH band fluxes in *ISO/SWS* spectra of no C_{60} -containing PNe.

Nebula	$F(\text{PAH } 3.3)$ ($\text{erg s}^{-1} \text{cm}^{-2}$)	$F(\text{PAH } 11.3)$ ($\text{erg s}^{-1} \text{cm}^{-2}$)	$F(3.3)/F(11.3)$
BD+30° 3639	6.28(−14)	2.34(−13)	0.27
Hubble5	1.88(−14)	9.02(−14)	0.21
Hen2-113	5.62(−14)	1.51(−13)	0.37
Hen3-1333	8.77(−14)	2.82(−13)	0.31
M1-78	2.10(−14)	8.32(−14)	0.25
M2-43	1.92(−14)	4.66(−14)	0.41
NGC6302	8.67(−15)	3.36(−14)	0.26
NGC6537	4.63(−15)	1.60(−14)	0.29
NGC7027	2.05(−13)	1.58(−12)	0.13
Vo1	1.41(−14)	3.95(−14)	0.36

sured the $F(3.3 \mu\text{m})/F(11.3 \mu\text{m})$ PAH intensity ratios of 10 other Galactic non- C_{60} PNe using their *ISO/SWS* spectra. These results are listed in Table 8. The average value is 0.29, consistent with the results by R. Ohsawa based on *AKARI/IRC* and *Spitzer/IRS* spectra of 16 Galactic non- C_{60} PNe (0.3; in private communication). Since the radiation field is probably roughly similar for all C_{60} -containing PNe and non- C_{60} PNe, the $F(3.3 \mu\text{m})/F(11.3 \mu\text{m})$ ratio is likely governed by the PAH size distribution. Thus, we conclude that our C_{60} -containing PNe have relatively smaller PAHs than non- C_{60} PNe.

Table 9. The 11 μm band fluxes of the emission and continuum components.

Nebula	$F(E)^a$ ($\text{erg s}^{-1} \text{cm}^{-2}$)	$F(C)^b$ ($\text{erg s}^{-1} \text{cm}^{-2}$)	$F(E)/F(C)$
Hen2-68	2.89(−11)	5.44(−11)	0.53 ± 0.01
IC418	1.24(−9)	1.90(−9)	0.65 ± 0.01
IC2501	5.63(−11)	1.59(−10)	0.35 ± 0.01
K3-62	4.91(−11)	1.06(−10)	0.46 ± 0.01
M1-6	9.42(−11)	1.36(−10)	0.69 ± 0.01
M1-9	9.04(−12)	2.15(−11)	0.42 ± 0.01
M1-11	4.22(−10)	6.17(−10)	0.68 ± 0.01
M1-12	6.93(−11)	1.18(−10)	0.59 ± 0.01
M1-20	4.74(−11)	5.64(−11)	0.84 ± 0.02
SaSt2-3	6.20(−13)	2.54(−12)	0.24 ± 0.01
Tc1	5.28(−11)	1.43(−10)	0.37 ± 0.01

^aThe sum of the band emission without continuum between 10.2 and 13.2 μm .

^bThe sum of the continuum between 10.2 and 13.2 μm .

4.7 The broad 11 μm feature

The appearance of the broad 11 μm feature is presented in Fig. 7a. The flux density is normalized to the peak flux density of the 18.9 μm C_{60} after the continuum was subtracted. The H I 11.3 and 12.4 μm , $[\text{S IV}]$ 10.51 μm , and $[\text{Ne II}]$ 12.81 μm lines are subtracted out using Multiple Gaussian fitting. Except for M1-11, the emission profiles show a nearly flat portion between 11.2 and 12.4 μm . The position of the 11.3 μm PAH band is indicated by the dotted line in Fig. 7a. The peak intensity of the 11 μm feature in SaSt2-3 and

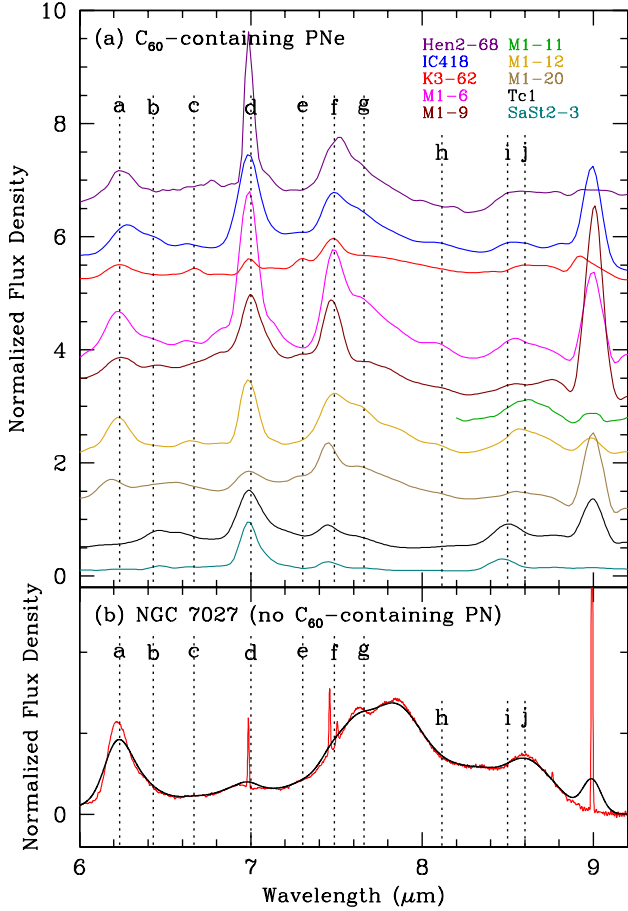


Figure 5. (upper panel) The continuum subtracted over 6.0-9.2 μm of all sources for which data is available in this range, normalized to the peak flux density of the 8.5 μm C_{60} +8.6 μm PAH band and then adjusted. The emission features seen in these spectra are indicated by dotted lines and lower-case letters. (lower panel) The *ISO/SWS* spectrum of the C-rich PN NGC7027. We removed the high-excitation lines such as [Cl v] 6.71 μm , He II 6.95 μm , [Na III] 7.32 μm , [Ne VI] 7.65 μm , [Ar V] 7.90 μm , [Na VI] 8.61 μm , and [K VI] 8.83 μm and the pure rotational transition lines of molecular hydrogen (H_2) lines from the original spectrum of NGC7027. The resolution of this spectrum was reduced to that of *Spitzer/IRS*. The original resolution spectrum is indicated by the red line and the degraded one is indicated by the black line. The emission features seen in these spectra are indicated by dotted lines and lower-case letters. a: PAH C=C stretch 6.23 μm , b: C_{60} + 6.4 μm (possible), c: C_{24} planar (possible) or PAH C=C stretch 6.67 μm , d: C_{60} 7.0 μm + [Ar II] 6.99 μm , e: an emission feature at 7.30 μm seen by Scott & Duley (1996); Scott et al. (1997), f: C_{60}^+ + H I 7.46 μm and the H I 7.50 μm complex, g: PAH C-C stretch 7.7 μm , h: C_{60}^+ 8.1 μm (possible), i: C_{60} 8.5 μm , and j: PAH C-H in-plane bend 8.6 μm .

Tc1, which show the prominent C_{60} bands, is much weaker than in the other PNe.

The band profile and the peak intensity in IC418, K3-62, M1-6, and M1-12 are very similar. The effective temperatures T_{eff} in these PNe are quite different (31 660-45 000 K), so we believe the 11 μm emission does not correlate with T_{eff} (Fig. 7b). We measured the integrated flux emission band $F(E)$ and the integrated flux $F(C)$ of the underlying continuum between 10.2 and 13.2 μm (Table 9). The flux of the emission band $F(E)$ includes the 11.3 μm emission. The error estimate of $F(E)$ and $F(C)$ is assumed to be equal to the standard deviation of continuum <10.2 and >13.2 μm . Fig. 7b shows the band strengths (defined as the ratio $F(E)/F(C)$) against

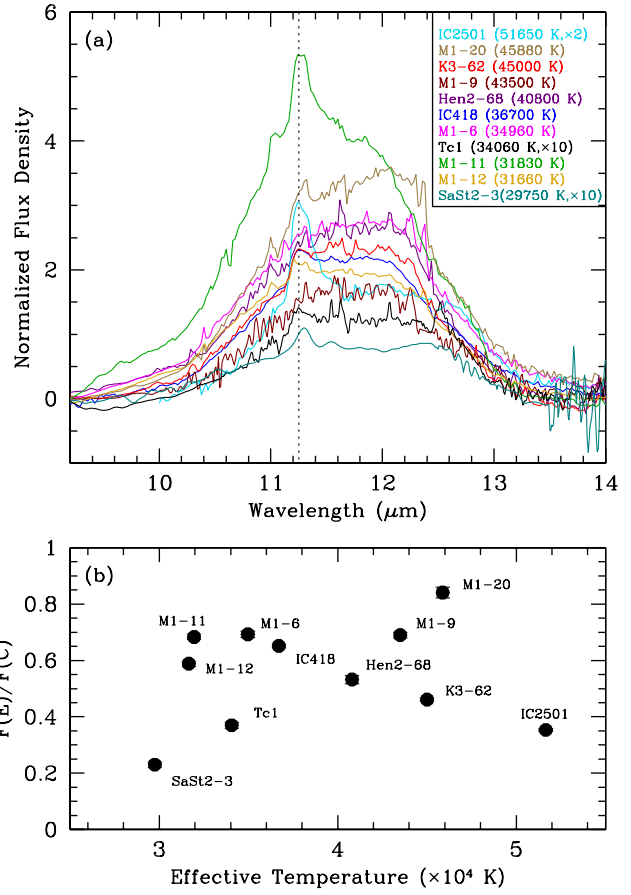


Figure 7. (upper) The continuum subtracted spectra over 9.1-14 μm , normalized to the peak flux density of C_{60} 18.9 μm , except for IC2501, SaSt2-3, and Tc1. The scaling factor for these PNe are 2, 10, and 10 after the normalization to C_{60} 18.9 μm . The position of the 11.3 μm PAH (or HAC) is indicated by the dotted line. (lower) The plot between the intensity and the effective temperatures of the central stars.

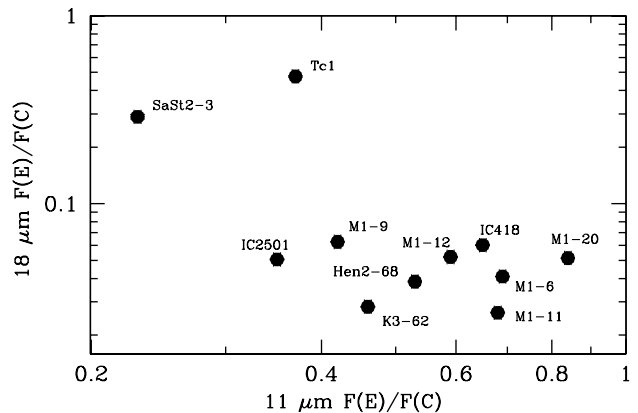


Figure 8. The correlation between the band strengths of the 18.9 μm C_{60} band and the broad 11 μm band.

Table 10. The 18.5-19.3 μm continuum fluxes and the 18.9 microns C_{60} band strength.

Nebula	$F(E)^a$ ($\text{erg s}^{-1} \text{cm}^{-2}$)	$F(C)^b$ ($\text{erg s}^{-1} \text{cm}^{-2}$)	$F(E)/F(C)$
Hen2-68	7.83(-13)	2.03(-11)	$3.85(-2) \pm 6.62(-3)$
IC418	4.44(-11)	7.38(-10)	$6.02(-2) \pm 2.82(-3)$
IC2501	3.93(-12)	7.78(-11)	$5.05(-2) \pm 7.85(-3)$
K3-62	1.32(-12)	4.66(-11)	$2.83(-2) \pm 3.58(-3)$
M1-6	1.98(-12)	4.83(-11)	$4.10(-2) \pm 2.28(-3)$
M1-9	4.19(-13)	2.07(-12)	$6.26(-2) \pm 5.33(-3)$
M1-11	6.89(-12)	2.62(-11)	$2.63(-2) \pm 4.45(-3)$
M1-12	2.41(-12)	4.62(-11)	$5.21(-2) \pm 2.71(-3)$
M1-20	8.74(-13)	1.70(-11)	$5.14(-2) \pm 5.65(-3)$
SaSt2-3	3.03(-13)	1.04(-12)	$2.90(-1) \pm 2.87(-2)$
Tc1	2.40(-11)	5.05(-11)	$4.76(-1) \pm 1.01(-2)$

^aThe 18.9 μm C_{60} fluxes. ^bThe continuum fluxes between 18.5 and 19.3 μm .

T_{eff} . The correlation coefficient between these two parameters is 0.10, meaning they are not correlated. Even if we exclude SaSt2-3 because the SNR of this object is much lower than those of the other PNe, the correlation coefficient is still small (-0.20). Thus, we confirm that there is no correlation between the 11 μm band strength and the T_{eff} of the central star.

The peak intensities of the broad 11 μm feature in SaSt2-3 and Tc1 are much lower than those in the other PNe. The relation between the 11 μm band and the 18.9 μm C_{60} band strength is of interest (Fig. 8). Bernard-Salas et al. (2012) demonstrated the similarity between the observed 6-14 μm spectra of C_{60} -containing PNe and the spectra of HAC/a-C:H particles, which shows strong emission around 11.3 μm (See Fig. 7 of Bernard-Salas et al. 2012). They concluded it likely to demonstrate a link between the fullerene formation process and the 6-9 and 10-13 μm broad bands. To check the relation between the 18 μm C_{60} and the 11 μm band strengths, we also measured the the integrated flux $F(C)$ of the underlying continuum between 18.5 and 19.2 μm , as listed in the third column of Table 10. We define the ratio of the 18.9 μm C_{60} band integrated flux to $F(C)$ as the 18.9 μm C_{60} band strength, and we plotted the diagram of the 18.9 μm C_{60} and 11 μm band strengths in Fig. 8, although careful treatment of the 18.9 μm C_{60} band strength of SaSt2-3 is necessary, as we explained in Section 4.2. No trend exists between the 11 μm band and the 18.9 μm C_{60} band strengths, suggesting that the heating mechanism of the C_{60} and the broad 11 μm bands is different.

4.8 The 30 μm feature and the cold dust continuum

All the sources in our sample show a clear broad emission feature around 30 μm , except for IC2501, for which we do not have any data $>20 \mu\text{m}$. The feature typically starts around 24 μm , and ends around 45 μm , outside of the *Spitzer*/IRS wavelength coverage, and it is carried by a solid state component. Its identification remains unclear. Hony et al. (2002) argued that the feature is due to MgS (magnesium sulfide), while rejecting other carriers, such as HACs. The MgS identification has been widely accepted by the community for the 30 μm feature seen in carbon-rich AGB stars, post-AGB stars and PNe (e.g. Zijlstra et al. 2006; Zhukovska & Gail 2008; Woods et al. 2011; Lombaert et al. 2012). However, Zhang et al. (2009) have demonstrated using energetic arguments that the abundance of MgS is not sufficient to explain the strength of the feature in post-AGB star HD56126, thus creating considerable doubt

Table 11. Wavelength ranges blocked in the spectrum of IC418, prior to continuum fitting.

Blocked range (μm)	Comment
<13.5	broad 11 μm and 11 μm PAH bands
15.5-16	[Ne III] 15.5 μm
17-18	17.4 μm C_{60} band and H I 17.61 μm
18.5-19.5	18.9 μm C_{60} band and [S III] 18.7 μm
23-45	30 μm feature
51-53	[O III] 51.8 μm
56-58	[N III] 57.3 μm
62-64	[O I] 63.2 μm
87-90	[O III] 88.4 μm
121-123	[N II] 121.8 μm
144-147	[O I] 145.5 μm
155-160	[C II] 157 μm

concerning the validity of the MgS identification. In a recent analysis of the 30 μm feature observed in a sample of extreme carbon stars, Messenger et al. (2013) search for a correlation between the 30 μm feature, and the 11.3 μm SiC (silicon carbide) feature, on the grounds that the 30 μm feature is likely carried by a carbide or sulfide component. They find that a correlation exists within specifically this class of objects, suggesting that the abundance of the carrier of the 30 μm feature is linked to the SiC abundance. Analysis of laboratory spectra shows that various types of sulfides, so not just MgS, all show a resonance at approximately the right wavelength (Messenger et al. 2013).

In this work, however, we explore the possibility that the 30 μm feature is due to the carrier of the dust continuum. The dust continuum in carbon-rich AGB stars and PNe is generally thought to be due to amorphous carbon (e.g. Srinivasan et al. 2010), but there are hints that graphite is more appropriate (e.g. Speck et al. 2009). Comparing the opacities of amorphous carbon and graphite shows that while amorphous carbon produces a featureless continuum, graphite exhibits a very broad, strong feature peaking around 40 μm , which shifts to longer wavelengths for larger grains (Draine & Lee 1984). The position of the feature also seems to be a function of the conductivity of graphite, and Jiang et al. (2013) show that for graphite with a d.c. conductivity of $100 \Omega^{-1} \text{cm}^{-1}$ the resonance is found at 30 μm . Therefore, if we accept that carbon in its crystalline form could produce a feature around 30-40 μm , and that the exact position of this feature may be dependent the grain properties, such as size and shape, we can investigate whether it is possible to construct a dust opacity that explains both the long-wavelength dust continuum and the strength of the 30 μm feature at the same time.

4.8.1 Deriving the opacity function using IC418

IC418 is the most suitable source to constrain the opacity function of the carrier responsible for both the continuum and the 30 μm feature, because it is the only source in our sample where spectroscopy is available at $\lambda > 40 \mu\text{m}$, allowing us to trace the full extent of the 30 μm feature, and have an additional stretch of continuum baseline at even longer wavelengths. The constructed opacity function can then be applied to the other objects in our sample.

First, we removed all emission lines from the spectrum of IC418, by blocking the data at the wavelength ranges listed in Table 11. All data with $\lambda < 13.5 \mu\text{m}$ has been blocked because of a change in slope due to contributions from hot dust and PAH emission. The remaining spectrum was then re-binned with a spectral resolution of $\Delta\lambda/\lambda=10$ to reduce the noise and make the spectrum

more smooth. All data points in the re-binned spectrum of IC418 were assigned a flux uncertainty of 5%, in line with typical values for the *Spitzer*/IRS and *ISO* flux calibration accuracy.

Assuming that dust in PNe is found to be present at a range of temperatures, reflecting a range of distances to the central star, we follow the method put forward by Kemper et al. (2002). This model assumes that dust is distributed around the central star following a power-law $\rho(r) \propto r^{-p}$, with the temperature distribution also follows a power-law $T(r) \propto r^{-q}$. Thus, following Kemper et al. (2002) we can derive, for spherical grains, that

$$F_\nu = C \cdot Q_{\text{abs}}(\lambda) \int_{T_{\text{min}}}^{T_{\text{max}}} T^{-\alpha} B_\lambda(T) dT \quad (2)$$

with $\alpha = (3 - p)/q > 0$. $Q_{\text{abs}}(\lambda)$ is the absorption efficiency as a function of wavelength. Relevant species that could contribute to the continuum are amorphous carbon and graphite, as discussed before, but also SiC. Both amorphous carbon and SiC essentially follow a power-law $\propto \lambda^{-\beta}$ for $\lambda > 13.5 \mu\text{m}$. Graphite does deviate from this power-law behavior due to the strong resonance around $40 \mu\text{m}$ which may be related to the $30 \mu\text{m}$ feature we are trying to fit. This means we can substitute $\lambda^{-\beta}$ for $Q_{\text{abs}}(\lambda)$ in Equation (2), which yields

$$F_\nu = C \cdot \lambda^{-\beta} \int_{T_{\text{min}}}^{T_{\text{max}}} T^{-\alpha} B_\lambda(T) dT \quad (3)$$

This equation is fitted to the re-binned spectral data of the continuum emission due to the dust in IC418 using the MPFIT algorithm (Markwardt 2009) excluding the wavelengths listed in Table 11. The fit is not very sensitive to the minimum temperature at the outskirts of the nebula, so we fix $T_{\text{min}}=20$ K, a temperature more or less characteristic for dust in the interstellar medium. This results in only four free parameters, namely, the maximum dust temperature T_{max} closest to the central star, the power-law index α , describing the physical properties of the nebula, the power-law index β describing the opacity function of the continuum and the scaling factor C .

4.8.2 Derivation of opacities

Due to the presence of two power-laws in Equation (3) (one over T , and one over λ) there is a certain amount of degeneracy in the resulting fit. Trial and error shows that α is approximately equal to unity, so we have fixed it at that value, to find that the index β describing the opacity power-law, is 1.20. The scaling factor $C=3.3(-10)$, and we find that the maximum temperature $T_{\text{max}}=155.3$ K.

We can use these fit parameters now as true values in Equation (2), while we leave $Q_{\text{abs}}(\lambda)$ as an unknown. Using the spectrum of IC418 with all emission lines and features, except the $30 \mu\text{m}$ feature, removed as $F_\nu(\lambda)$, we can derive $Q_{\text{abs}}(\lambda)$. The result is a table of Q values over a range from 13.5 to $\sim 150 \mu\text{m}$, which we have re-binned with a spectral resolution of $\lambda/\Delta\lambda=10$. The derived opacity for the $30 \mu\text{m}$ feature and the continuum together is shown in Fig. 9 with the red line, along with a $\lambda^{-1.2}$ power-law in black. Outside the $30 \mu\text{m}$ feature, the derived opacity follows the power-law quite closely, and is therefore able to reproduce the continuum emission. Note that the derived opacity is given in arbitrary units, because we did not specify any grain size or shape. The mass contained in this component can therefore not be derived.

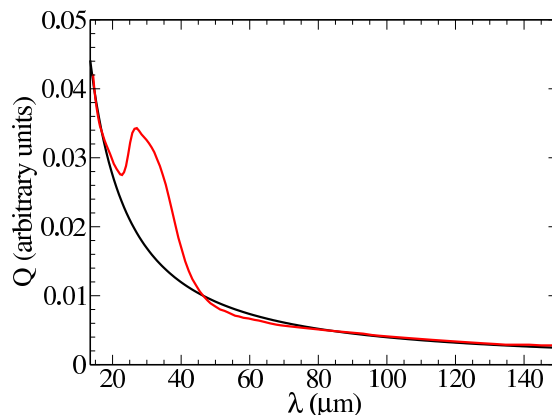


Figure 9. The derived opacity for the carrier of the continuum and the $30 \mu\text{m}$ feature (red), compared to a power-law opacity $\propto \lambda^{-1.2}$ (black). The Q -values are in arbitrary units.

Table 12. Fit parameters for all sources, for the solution to Equation 2, using the joint opacity presented in Fig. 9 for Q_{abs} .

Nebula	T_{max} (K)	C
Hen2-68	139.1 ± 0.1	2.57(-11)
IC418	146.1 ± 0.1	6.70(-10)
K3-62	138.5 ± 0.2	5.86(-11)
M1-6	150.3 ± 0.2	3.58(-11)
M1-9	147.0 ± 0.9	5.91(-12)
M1-11	149.5 ± 0.1	2.00(-10)
M1-12	140.8 ± 0.1	4.77(-11)
M1-20	148.1 ± 0.1	1.33(-11)
SaS2-3	148.9 ± 0.1	9.00(-13)
Tc1	117.2 ± 0.1	1.75(-10)

4.8.3 Fitting the $30 \mu\text{m}$ feature in the entire sample

The joint opacity $Q_{\text{abs}}(\lambda)$, shown in Fig. 9, can be used in Equation (2) to fit the continuum and $30 \mu\text{m}$ emission in all sources in the sample. Again, we treat T_{max} and C as free parameters. Experience shows that α always has a value close to unity, so we fixed this parameter at that value. The equation was solved using the MPFIT routine (Markwardt 2009), and the results for all targets in our sample is shown in Table 12 and Fig. 10. The first column of Table 12 gives the source name, the second column the fitted T_{max} , and the third column the scaling factor C . In Fig. 10, the spectra are shown in black, and the photometry points with blue crosses. The photometry comes from the four *WISE* bands ($\lambda_c=3.4, 4.6, 11.6$, and $22.1 \mu\text{m}$) and the *AKARI*/IRC & FIS bands ($9.2, 19.8, 66.7$, and $89.2 \mu\text{m}$). The red line shows the best fit result to Equation (2), which was fit to the data to the right of the dashed line, e.g. with $\lambda > 13.5 \mu\text{m}$. The best fit modified black-body, e.g. a single temperature black-body multiplied by a λ^{-p} emissivity law, to the same data is shown for comparison with a green line. For clarity, the spectra of M1-11 and Tc1 are shifted by the indicated factor. The uncertainties on the derived maximum temperature are of the order of 0.1–0.9 K, while the scaling factor is simply a linear factor applied to minimize the χ^2 values, and hence has an uncertainty of less than 1 %.

Fig. 10 shows that for all sources in our sample we can achieve a good fit to the $30 \mu\text{m}$ feature and continuum at the same time, us-

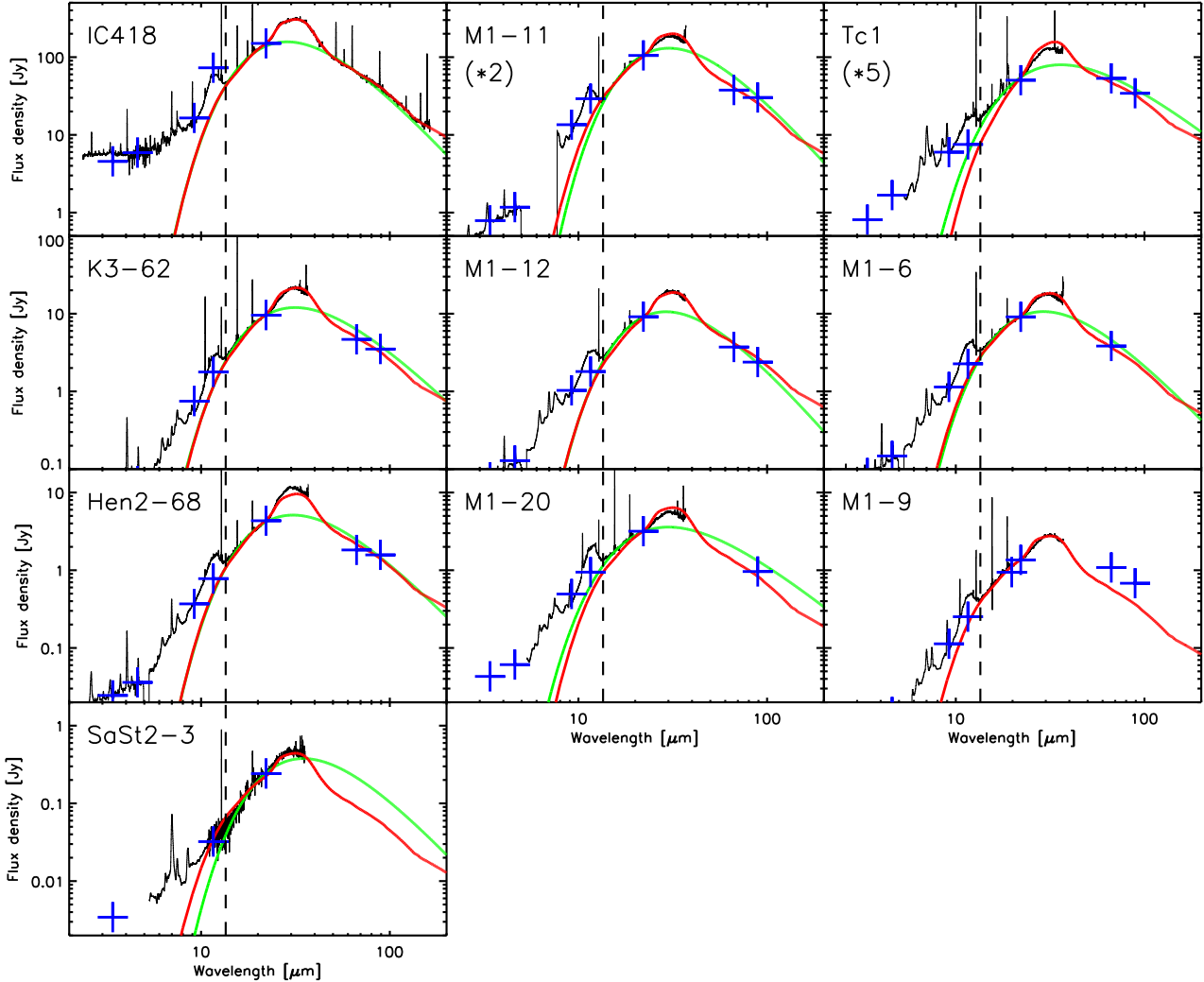


Figure 10. The best fit results for each of the objects to the continuum emission beyond $13.5 \mu\text{m}$, and the $30 \mu\text{m}$ feature. The spectra are shown in black, and the photometry points with blue crosses. The red line shows the best fit result to Equation (2), which was fit to the data to the right of the dashed line, e.g. with $\lambda > 13.5 \mu\text{m}$. The best fit modified blackbody, e.g. a single temperature blackbody multiplied by a λ^{-p} emissivity law, to the same data is shown for comparison in each of the panels with a green line. For clarity, the spectra of M1-11 and Tc1 are shifted by the indicated factor.

ing the opacity table derived from the full spectrum of IC418 (Fig. 9), and by applying the emission model described in Equation (2). Therefore, the fit results for our sample are consistent with having a single carrier for the continuum emission ($> 13.5 \mu\text{m}$) and the $30 \mu\text{m}$ feature. The exact composition of this material remains unknown at this time, but we speculate that it may be related to HAC or graphite, because these species are known to have features in this wavelength range (Grishko et al. 2001; Draine & Lee 1984; Jiang et al. 2013). The opacity plot (Fig. 9) provides a starting point for future attempts to identify the material responsible for the continuum and the $30 \mu\text{m}$ feature.

5 DISCUSSION

5.1 Fullerenes in Galactic PNe

Out of 338 Galactic PNe observed with the *Spitzer*/IRS spectroscopic modules, we found a total of eleven objects in which C_{60}

is present using the SH data, six of which (Hen2-68, IC2501, K3-62, M1-6, M1-9, and SaSt2-3) are new detections. These eleven sources were identified by the presence of the 17.4 and $18.9 \mu\text{m}$ C_{60} resonances. SaSt2-3 and Tc1 also clearly show strong features at 7.0 and $8.5 \mu\text{m}$ due to C_{60} . Except for SaSt2-3 and Tc1, the $8.5 \mu\text{m}$ C_{60} band is heavily contaminated by the $8.6 \mu\text{m}$ PAH band.

The large number of Galactic PNe checked for the presence of C_{60} represent a considerable fraction of the total number of known (C-rich and O-rich) PNe in the Milky Way (~ 1200 ; Acker et al. 1992), thus, from this representative sample, we may conclude that the detectable presence of C_{60} is rather rare, with a detection rate of one out of ~ 30.7 PNe ($=338/11$).

Among our 338 PNe, the distances to 264 objects were measured by Stanghellini & Haywood (2010). Using their results, we plot the positions of these PNe on a face-on map of the Milky Way shown in Fig. 11. The positions of the spiral arms are taken from Cordes & Lazio (2002). Stanghellini & Haywood (2010) did not measure the distance to SaSt2-3, therefore we assumed the distance of 6 kpc , as earlier mentioned. Most PNe are concentrated

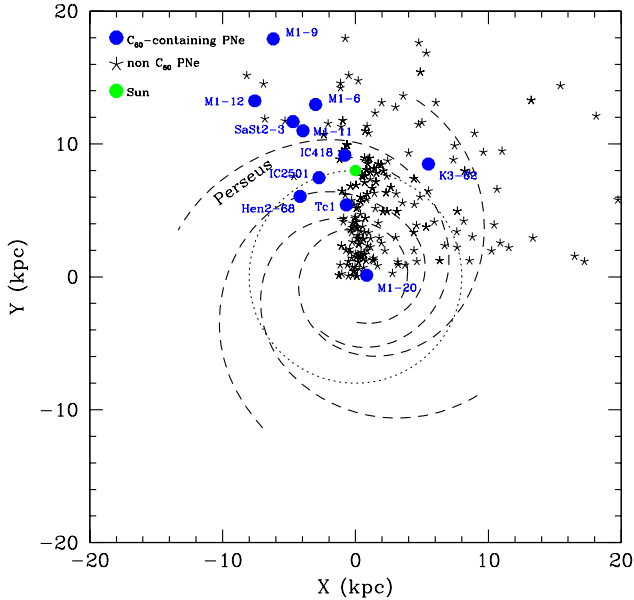


Figure 11. The positions of the 254 non- C_{60} (asterisks) and the 11 C_{60} PNe (filled blue circles) on a face-on map of the Milky Way. The position of the Sun is indicated by the filled green circle. The solar circle is indicated by the dotted line.

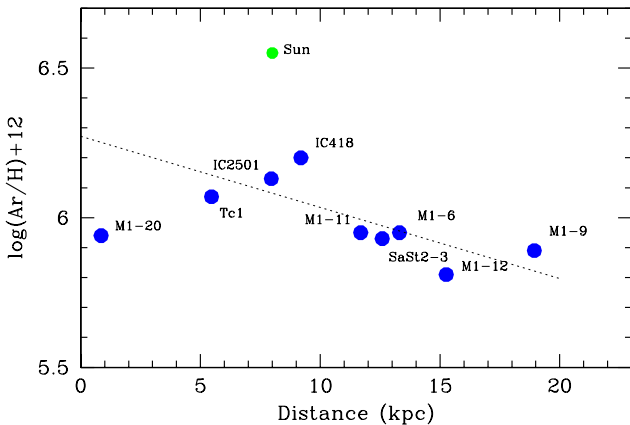


Figure 12. The diagram between the distance from the Galactic center and the Ar abundances of our sample. The dotted line is the relation established among our sample, except for M1-20.

to the Galactic center, however, there are very few C_{60} -containing PNe located in that direction, only M1-20 (in the Galactic bulge) and Tc1. Most of the C_{60} -containing PNe are in the Galactic anti-center and they are predominantly located in the region beyond the Perseus spiral arm.

In Fig. 12, we plotted the diagram of the Galactocentric distance against the Ar abundances of C_{60} -containing PNe. To investigate whether progenitor stars of C_{60} -containing PNe are initially metal-rich, we used Ar as a metallicity because Ar is not synthesized in low-mass AGB stars. The dotted line in Fig. 12 is the relation established between our sample, except for M1-20 and it is represented by

$$\text{Ar} = (-0.02 \pm 0.01) D_{gal} + (6.27 \pm 0.10), \quad (4)$$

where D_{gal} is the Galactocentric distance in kpc. The correla-

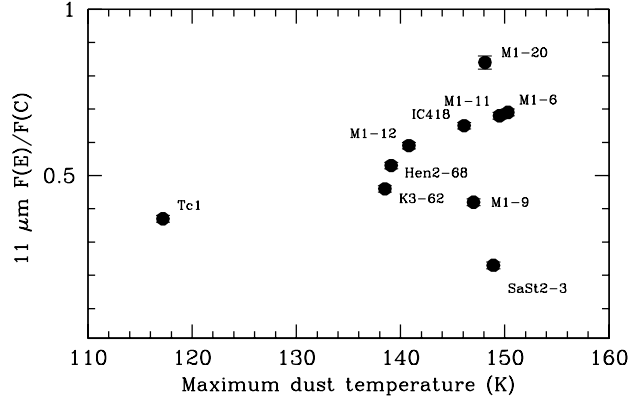


Figure 13. The plot between the band strength of the broad $11 \mu\text{m}$ band and the maximum dust temperature T_{max} .

tion factor is -0.48 . Our Ar gradient (-0.02) estimated by fitting to our sample is consistent with the result by Henry et al. (2004), who investigated the Ar abundance gradient using Galactic disk PN abundances. They reported that their correlation was $(-0.03 \pm 0.01) D_{gal} + (6.58 \pm 0.079)$. Their measured Ar abundances in PNe located around $D_{gal} = 5$ kpc and 10 kpc seem to be from ~ 6.3 to ~ 6.8 dex and from ~ 6 to ~ 6.5 dex, respectively. Therefore, we can conclude that C_{60} PNe are relatively metal-poor.

The O abundance amongst our sample can be represented by

$$\text{O} = (-0.02 \pm 0.01) D_{gal} + (8.64 \pm 0.10). \quad (5)$$

The correlation factor is -0.54 . Henry et al. (2004) reported a slope of -0.037 ± 0.008 and an intercept of 8.97 ± 0.069 . We need to be careful when interpreting the value derived for the O abundance; because O is slightly increased by the helium-burning and the third dredge-up during the AGB phase, its abundance does not indicate the initial metallicity. We can conclude that C_{60} PNe are relatively metal-poor objects even if O is increased during the AGB phase.

If our predicted C abundances are correct, the C/O ratio in our sample is increasing as D_{gal} is increasing. Therefore, that is a reason why most the C_{60} PNe are located outside the solar circle. To verify this, we need to measure the C/O ratio using the same type of emission-lines in the future.

5.2 The nature of the carrier of the $11 \mu\text{m}$ band

We have shown in Section 4.7 that the $11 \mu\text{m}$ band emission does not correlate with the C_{60} emission or the central star's effective temperature. However, when we plot $F(E)/F(C)$ against the $T_{\text{max}}(\text{dust})$ derived in Section 4.8, we find that the $11 \mu\text{m}$ band strength feature seems to scale with the thermal dust emission, as shown in Fig. 13, if we exclude the noisy spectrum of SaSt2-3. The correlation coefficients are 0.69 without SaSt2-3 and 0.39 with SaSt2-3, respectively. This correlation suggests that the carrier of this feature is a thermally heated dust component. On the other hand, substructure in the $11 \mu\text{m}$ feature at $11.3 \mu\text{m}$ points to a carrier that is related to PAHs. A similar broad feature is seen in Magellanic Cloud PNe, where it is thought to contain contributions from thermal emission from SiC and stochastically heated PAHs and PAH-like species (Bernard-Salas et al. 2009).

Table 13. Integrated fluxes of the dust continuum in 10.2-200 μm and C_{60} 17.4 and 18.9 μm emissions.

Nebula	$F(\text{dust})$ ($\text{erg s}^{-1} \text{cm}^{-2}$)	$F(C_{60})$ ($\text{erg s}^{-1} \text{cm}^{-2}$)	$F(C_{60})/F(\text{dust})$ ($\times 10^{-2}$)
Hen2-68	8.87(-10)	1.18(-12)	0.13
IC418	2.92(-8)	6.48(-11)	0.22
K3-62	1.98(-9)	1.92(-12)	0.10
M1-6	1.82(-9)	2.93(-12)	0.16
M1-9	2.62(-10)	6.34(-13)	0.24
M1-11	9.71(-9)	1.05(-11)	0.11
M1-12	1.80(-9)	3.50(-12)	0.19
M1-20	6.52(-10)	1.31(-12)	0.20
SaSt2-3	4.06(-11)	4.71(-13)	1.16
Tc1	2.71(-9)	3.24(-11)	1.20

5.3 Relative fraction of the 17.4 and 18.9 μm C_{60} band flux to the dust continuum flux

By combining the best fits for the 13.5-200 μm SED presented in Fig. 10 and the spline function fits for the 5.3-23 μm continuum, we estimated the integrated dust continuum flux in 10.2-200 μm . We estimated the integrated fluxes in 22.7-200 μm and in 10.2-22.7 μm by using the former and latter ones, respectively, and then we simply summed these fluxes. The integrated dust continuum $F(\text{dust})$ is listed in the second column of Table 13. The subsequent two columns are the total flux of the 17.4 and 18.9 μm emissions $F(C_{60})$ and its fraction with respect to $F(\text{dust})$. The high $F(C_{60})/F(\text{dust})$ also indicates that SaSt2-3 and Tc1 are unusually C_{60} -rich.

6 SUMMARY

We examined the properties of the nebulae, the central stars, and the infrared spectroscopic features in eleven Galactic C_{60} -bearing PNe based on ground-based and space telescope data, and theoretical models. Six of the sources in our sample (Hen2-68, IC2501, K3-62, M1-6, M1-9, and SaSt2-3) are newly identified as C_{60} -containing PNe. Photo-ionization models indicate that the nebular chemical abundance pattern and the current evolutionary status of the central stars are very similar, strongly suggesting that these C_{60} -bearing PNe have evolved from progenitors with similar initial mass and chemical composition. We found that the chemical abundances of C_{60} -containing PNe can be explained by AGB nucleosynthesis models for initially 1.5-2.5 M_{\odot} stars with $Z=0.004$. Their metallicity suggests that the progenitors are from an older population. We plotted the locations of the C_{60} -containing PNe on a face-on map of the Milky Way and we found that most of these PNe are outside the solar circle, consistent with low metallicity values. The effective temperatures differ from source to source, ranging from 29 750 to 51 650 K. There is no common characteristic in the nebular shape. Among the eleven PNe, SaSt2-3 and Tc1 clearly show strong C_{60} bands at 7.0 and 8.5 μm , while all eleven objects exhibit the 17.4 and 18.9 μm C_{60} features. The flux ratio between the 17.4 and 18.9 μm C_{60} feature is rather constant amongst the sample, with an average value of 0.49. The PAH profile over 6-9 μm in our sample is of the more chemically-processed class A. We estimated the number of C-atoms in typical PAHs using the ratio of the 3.3 μm to the 11.3 μm PAH flux. The number of C-atoms per PAH in C_{60} -containing PNe is small, compared to that in non- C_{60} PNe. We studied the nature of the 11 and 30 μm features. Both are showing to be due to thermal dust emission. The 11 μm band may have a contribution due to stochastically heated PAHs, while the

carrier of the 30 μm feature is shown to be one and the same as the carrier of the dust continuum.

ACKNOWLEDGMENTS

We are grateful to the anonymous referee for the useful suggestions which greatly improved this article. We thank Elisabetta Micelotta and Anthony Jones for numerous fruitful discussions. MO thanks the astronomy group at the University of Western Ontario for their kind support during his visit. FK acknowledges support from the National Science Council in the form of grant NSC100-2112-M-001-023-MY3. JBS wishes to acknowledge the support from a Marie Curie Intra-European Fellowship within the 7th European Community Framework Program under project number 272820. JC and EP acknowledge support from an NSERC Discovery Grant and a startup grant from the Department of Physics and Astronomy at Western University. This work is based on archival data obtained with the Spitzer Space Telescope, which is operated by the Jet Propulsion Laboratory, California Institute of Technology under a contract with NASA. Support for this work was provided by an award issued by JPL/Caltech. This work is in part based on *HST* archive data from the CADC and ESO archive data. This work is in part based on observations with *AKARI*, a JAXA project with the participation of ESA. This research has made grateful use of the SIMBAD database, operated at CDS, Strasbourg, France; and of NASA's Astrophysics Data System Bibliographic Services.

REFERENCES

- Acker A., Marcout J., Ochsenbein F., Stenholm B., Tylenda R., Schöhn C., 1992, The Strasbourg-ESO Catalogue of Galactic Planetary Nebulae. Parts I, II. Observatoire de Strasbourg
- Acker A., Neiner C., 2003, *A&A*, 403, 659
- Allamandola L. J., Tielens A. G. G. M., Barker J. R., 1989, *ApJ Supplements*, 71, 733
- Bernard-Salas J., Cami J., Peeters E., Jones A. P., Micelotta E. R., Groenewegen M. A. T., 2012, *ApJ*, 757, 41
- Bernard-Salas J., Peeters E., Sloan G. C., Gutenkunst S., Matsuura M., Tielens A. G. G. M., Zijlstra A. A., Houck J. R., 2009, *ApJ*, 699, 1541
- Boersma C., Bouwman J., Lahuis F., van Kerckhoven C., Tielens A. G. G. M., Waters L. B. F. M., Henning T., 2008, *A&A*, 484, 241
- Cahn J. H., Kaler J. B., Stanghellini L., 1992, *A&AS*, 94, 399
- Cami J., Bernard-Salas J., Peeters E., Malek S. E., 2010, *Science*, 329, 1180
- Clayton G. C., De Marco O., Whitney B. A., Babler B., Gallagher J. S., Nordhaus J., Speck A. K., Wolff M. J., Freeman W. R., Camp K. A., Lawson W. A., Roman-Duval J., Misselt K. A., Meade M., Sonneborn G., Matsuura M., Meixner M., 2011, *AJ*, 142, 54
- Cordes J. M., Lazio T. J. W., 2002, *ArXiv Astrophysics e-prints*
- Dopita M. A., Hua C. T., 1997, *ApJ Supplements*, 108, 515
- Draine B. T., Lee H. M., 1984, *ApJ*, 285, 89
- Draine B. T., Li A., 2007, *ApJ*, 657, 810
- Evans A., van Loon J. T., Woodward C. E., Gehrz R. D., Clayton G. C., Helton L. A., Rushton M. T., Eyres S. P. S., Krautter J., Starrfield S., Wagner R. M., 2012, *MNRAS*, 421, L92
- Ferland G. J., Korista K. T., Verner D. A., Ferguson J. W., Kingdon J. B., Verner E. M., 1998, *PASP*, 110, 761

- García-Hernández D. A., Iglesias-Groth S., Acosta-Pulido J. A., Manchado A., García-Lario P., Stanghellini L., Villaver E., Shaw R. A., Cataldo F., 2011a, *ApJ Letters*, 737, L30
- García-Hernández D. A., Kameswara Rao N., Lambert D. L., 2011b, *ApJ*, 729, 126
- García-Hernández D. A., Manchado A., García-Lario P., Stanghellini L., Villaver E., Shaw R. A., Szczerba R., Perea-Calderón J. V., 2010, *ApJ Letters*, 724, L39
- Gielen C., Cami J., Bouwman J., Peeters E., Min M., 2011, *A&A*, 536, A54
- Grishko V. I., Tereszchuk K., Duley W. W., Bernath P., 2001, *ApJ Letters*, 558, L129
- Henry R. B. C., Kwitter K. B., Balick B., 2004, *AJ*, 127, 2284
- Henry R. B. C., Kwitter K. B., Jaskot A. E., Balick B., Morrison M. A., Milingo J. B., 2010, *ApJ*, 724, 748
- Higdon S. J. U., Devost D., Higdon J. L., Brandl B. R., Houck J. R., Hall P., Barry D., Charmandaris V., Smith J. D. T., Sloan G. C., Green J., 2004, *PASP*, 116, 975
- Hony S., Waters L. B. F. M., Tielens A. G. G. M., 2002, *A&A*, 390, 533
- Houck J. R., Roellig T. L., van Cleve J., Forrest W. J., Herter T., Lawrence C. R., Matthews K., Reitsema H. J., Soifer B. T., Watson D. M., Weedman D., Huisjen M., Troeltzsch J., Barry D. J., Bernard-Salas J., Blacken C. E., Brandl B. R., Charmandaris V., Devost D., Gull G. E., Hall P., Henderson C. P., Higdon S. J. U., Pirger B. E., Schoenwald J., Sloan G. C., Uchida K. I., Appleton P. N., Armus L., Burgdorf M. J., Fajardo-Acosta S. B., Grillmair C. J., Ingalls J. G., Morris P. W., Teplitz H. I., 2004, *ApJ Supplements*, 154, 18
- Hubeny I., Lanz T., 1995, *ApJ*, 439, 875
- Jiang B., Li A., Liu J., J. Gao A. M., 2013, in *IAU Symposium*, Vol. 297, *Diffuse Interstellar Bands*, Cami J., Cox N., eds.
- Karakas A. I., 2010, *MNRAS*, 403, 1413
- Kemper F., Molster F. J., Jäger C., Waters L. B. F. M., 2002, *A&A*, 394, 679
- Kondratyeva L. N., 2003, *Astronomical and Astrophysical Transactions*, 22, 181
- Kroto H. W., Heath J. R., O'Brien S. C., Curl R. F., Smalley R. E., 1985, *Nature*, 318, 162
- Lodders K., 2003, *ApJ*, 591, 1220
- Lombaert R., de Vries B. L., de Koter A., Decin L., Min M., Smolders K., Mutschke H., Waters L. B. F. M., 2012, *A&A*, 544, L18
- Markwardt C. B., 2009, in *Astronomical Society of the Pacific Conference Series*, Vol. 411, *Astronomical Data Analysis Software and Systems XVIII*, Bohlender D. A., Durand D., Dowler P., eds., p. 251
- Messenger S. J., Speck A., Volk K., 2013, *ApJ*, 764, 142
- Micelotta E. R., Jones A. P., Cami J., Peeters E., Bernard-Salas J., Fanchini G., 2012, *ApJ*, 761, 35
- Morisset C., Georgiev L., 2009, *A&A*, 507, 1517
- Morisset C., Szczerba R., Anibal García-Hernández D., García-Lario P., 2012, in *IAU Symposium*, Vol. 283, *IAU Symposium*, pp. 452–453
- Murakami H., Baba H., Barthel P., Clements D. L., Cohen M., Doi Y., Enya K., Figueredo E., Fujishiro N., Fujiwara H., Fujiwara M., Garcia-Lario P., Goto T., Hasegawa S., Hibi Y., Hirao T., Hiromoto N., Hong S. S., Imai K., Ishigaki M., Ishiguro M., Ishihara D., Ita Y., Jeong W.-S., Jeong K. S., Kaneda H., Kataza H., Kawada M., Kawai T., Kawamura A., Kessler M. F., Kester D., Kii T., Kim D. C., Kim W., Kobayashi H., Koo B. C., Kwon S. M., Lee H. M., Lorente R., Makiuti S., Matsuhara H., Matsumoto T., Matsuo H., Matsuura S., Müller T. G., Murakami N., Nagata H., Nakagawa T., Naoi T., Narita M., Noda M., Oh S. H., Ohnishi A., Ohyama Y., Okada Y., Okuda H., Oliver S., Onaka T., Ootsubo T., Oyabu S., Pak S., Park Y.-S., Pearson C. P., Rowan-Robinson M., Saito T., Sakon I., Salama A., Sato S., Savage R. S., Serjeant S., Shibai H., Shirahata M., Sohn J., Suzuki T., Takagi T., Takahashi H., Tanabé T., Takeuchi T. T., Takita S., Thomson M., Uemizu K., Ueno M., Usui F., Verdugo E., Wada T., Wang L., Watabe T., Watarai H., White G. J., Yamamura I., Yamauchi C., Yasuda A., 2007, *PASJ*, 59, 369
- Onaka T., Matsuhara H., Wada T., Fujishiro N., Fujiwara H., Ishigaki M., Ishihara D., Ita Y., Kataza H., Kim W., Matsumoto T., Murakami H., Ohyama Y., Oyabu S., Sakon I., Tanabé T., Takagi T., Uemizu K., Ueno M., Usui F., Watarai H., Cohen M., Enya K., Ootsubo T., Pearson C. P., Takeyama N., Yamamuro T., Ikeda Y., 2007, *PASJ*, 59, 401
- Otsuka M., Kemper F., Hyung S., Sargent B. A., Meixner M., Tajitsu A., Yanagisawa K., 2013, *ApJ*, 764, 77
- Otsuka M., Tajitsu A., Hyung S., Izumiura H., 2010, *ApJ*, 723, 658
- Patriarchi P., Cerruti-Sola M., Perinotto M., 1989, *ApJ*, 345, 327
- Peeters E., Honny S., Van Kerckhoven C., Tielens A. G. G. M., Allamandola L. J., Hudgins D. M., Bauschlicher C. W., 2002, *A&A*, 390, 1089
- Peeters E., Tielens A. G. G. M., Allamandola L. J., Wolfire M. G., 2012, *ApJ*, 747, 44
- Pereira C.-B., Miranda L.-F., 2007, *A&A*, 467, 1249
- Pottasch S. R., Bernard-Salas J., 2006, *A&A*, 457, 189
- Pottasch S. R., Surendiranath R., Bernard-Salas J., 2011, *A&A*, 531, A23
- Preite-Martinez A., Acker A., Koeppen J., Stenholm B., 1989, *A&AS*, 81, 309
- Ricca A., Bauschlicher Jr. C. W., Boersma C., Tielens A. G. G. M., Allamandola L. J., 2012, *ApJ*, 754, 75
- Roberts K. R. G., Smith K. T., Sarre P. J., 2012, *MNRAS*, 421, 3277
- Schutte W. A., Tielens A. G. G. M., Allamandola L. J., 1993, *ApJ*, 415, 397
- Scott A., Duley W. W., 1996, *ApJ Letters*, 472, L123
- Scott A. D., Duley W. W., Jahani H. R., 1997, *ApJ Letters*, 490, L175
- Sellgren K., Werner M. W., Ingalls J. G., Smith J. D. T., Carleton T. M., Joblin C., 2010, *ApJ Letters*, 722, L54
- Sharpee B., Zhang Y., Williams R., Pellegrini E., Cavagnolo K., Baldwin J. A., Phillips M., Liu X.-W., 2007, *ApJ*, 659, 1265
- Sloan G. C., Jura M., Duley W. W., Kraemer K. E., Bernard-Salas J., Forrest W. J., Sargent B., Li A., Barry D. J., Bohac C. J., Watson D. M., Houck J. R., 2007, *ApJ*, 664, 1144
- Sloan G. C., Keller L. D., Forrest W. J., Leibensperger E., Sargent B., Li A., Najita J., Watson D. M., Brandl B. R., Chen C. H., Green J. D., Markwick-Kemper F., Herter T. L., D'Alessio P., Morris P. W., Barry D. J., Hall P., Myers P. C., Houck J. R., 2005, *ApJ*, 632, 956
- Speck A. K., Corman A. B., Wakeman K., Wheeler C. H., Thompson G., 2009, *ApJ*, 691, 1202
- Srinivasan S., Sargent B. A., Matsuura M., Meixner M., Kemper F., Tielens A. G. G. M., Volk K., Speck A. K., Woods P. M., Gordon K., Marengo M., Sloan G. C., 2010, *A&A*, 524, A49
- Stanghellini L., Haywood M., 2010, *ApJ*, 714, 1096
- Storey P. J., Hummer D. G., 1995, *MNRAS*, 272, 41
- Tajitsu A., Tamura S., 1998, *AJ*, 115, 1989
- Vassiliadis E., Wood P. R., 1994, *ApJ Supplements*, 92, 125
- Wang W., Liu X.-W., 2007, *MNRAS*, 381, 669

Weidmann W. A., Gamen R., 2011a, A&A, 531, A172
 —, 2011b, A&A, 526, A6
 Williams R., Jenkins E. B., Baldwin J. A., Zhang Y., Sharpee B., Pellegrini E., Phillips M., 2008, ApJ, 677, 1100
 Woods P. M., Oliveira J. M., Kemper F., van Loon J. T., Sargent B. A., Matsuura M., Szczerba R., Volk K., Zijlstra A. A., Sloan G. C., Lagadec E., McDonald I., Jones O., Gorjian V., Kraemer K. E., Gielen C., Meixner M., Blum R. D., Sewilo M., Riebel D., Shiao B., Chen C.-H. R., Boyer M. L., Indebetouw R., Antoniou V., Bernard J.-P., Cohen M., Dijkstra C., Galametz M., Galliano F., Gordon K. D., Harris J., Hony S., Hora J. L., Kawamura A., Lawton B., Leisenring J. M., Madden S., Marengo M., McGuire C., Mulia A. J., O'Halloran B., Olsen K., Paladini R., Paradis D., Reach W. T., Rubin D., Sandstrom K., Soszyński I., Speck A. K., Srinivasan S., Tielens A. G. G. M., van Aarle E., van Dyk S. D., van Winckel H., Vijn U. P., Whitney B., Wilkins A. N., 2011, MNRAS, 411, 1597
 Zhang C. Y., Kwok S., 1993, ApJ Supplements, 88, 137
 Zhang K., Jiang B. W., Li A., 2009, ApJ, 702, 680
 Zhang Y., Kwok S., 2011, ApJ, 730, 126
 Zhukovska S., Gail H.-P., 2008, A&A, 486, 229
 Zijlstra A. A., Matsuura M., Wood P. R., Sloan G. C., Lagadec E., van Loon J. T., Groenewegen M. A. T., Feast M. W., Menzies J. W., Whitelock P. A., Blommaert J. A. D. L., Cioni M. R. L., Habing H. J., Hony S., Loup C., Waters L. B. F. M., 2006, MNRAS, 370, 1961

APPENDIX A: FLUX MEASUREMENTS OF THE 7.0 AND 8.5 MICRONS C₆₀ BAND

As mentioned in Sections 2.2 and 4.3, all C₆₀-containing PNe in our sample show PAH features. Therefore, we assumed that the emission line around 8.5 μm is not only due to C₆₀, but also shows a contribution due to the 8.6 μm PAH band. We measured the C₆₀ band in SaSt2-3 and Tc1 using a single Gaussian, thus obtaining the FWHM of the 8.5 μm C₆₀ band. In a multiple Gaussian fit to the 8.5 μm C₆₀ and 8.6 μm PAH complex in PNe except for SaSt2-3 and Tc1, we adopted the average FWHM of the 8.5 μm C₆₀ in SaSt2-3 and Tc1 (~0.18 μm) as the first assumption for the 8.5 μm C₆₀ component. We fix the FWHM of the 8.6 μm PAH band at the value of 0.23 μm measured from the ISO/SWS spectrum of NGC7027 displayed in Fig. 5b.

Measurements of the 7.0 μm C₆₀ band are more difficult. To investigate the excitation mechanism of C₆₀, flux measurements of the 7.0 μm C₆₀ bands with any contamination subtracted are necessary, as discussed by Bernard-Salas et al. (2012). The 7.0 μm C₆₀ band is mainly contaminated by the [Ar II] 6.99 μm line. We do not detect any pure rotational H₂ lines in any of the spectra, so we assume that the contribution from the H₂ v=0-0 S(5) 6.91 μm line is negligibly small. In NGC7027, the flux ratio of the 6.92 μm aliphatic band to the 6.2 μm PAH band is 0.12.

We estimated the flux in the 7.0 μm C₆₀ resonance by deconstructing the observed 7.0 μm band in its components due to the 6.92 μm aliphatic band, the [Ar II] 6.99 μm line, and the 7.0 μm C₆₀ combination. We assumed that the flux ratio of the 6.92 μm to 6.2 μm PAH bands (0.12) is the same as in NGC7027 and the flux ratio of [Ar II] 6.99 μm to [Ar III] 8.99 μm derived with CLOUDY (See Table 3). The predicted ratio of $F([\text{Ar II}] 6.99 \mu\text{m})/F([\text{Ar III}] 8.99 \mu\text{m})$ is in the last column. The values in Hen2-68 and K3-62 are estimated using a relation between the ratio and T_{eff} among our

PNe with >36 000 K;

$$F([\text{Ar II}] 6.99 \mu\text{m})/F([\text{Ar III}] 8.99 \mu\text{m}) = -1.35 \times 10^{-4} T_{\text{eff}} + 6.16. \quad (\text{A1})$$

The predicted line ratio, in combination with the measured flux for the [Ar III] 8.99 μm line, was used to estimate the contamination from [Ar II] 6.99 μm line to C₆₀ 7.0 μm feature.

The total flux of the 7.0 μm complex ($F_{\text{tot.}}(7.0\mu\text{m})$) is simply the sum of the [Ar II] 6.99 μm ($F(6.99 \mu\text{m})$), the 6.92 μm aliphatic band ($F(6.92 \mu\text{m})$), and the C₆₀ 7.0 μm band ($F_{\text{C}_{60}}(7.0 \mu\text{m})$). Thus, the approximate flux of the 7.0 μm C₆₀ line can be written as

$$F_{\text{C}_{60}}(7.0 \mu\text{m}) = F_{\text{tot.}}(7.0 \mu\text{m}) - \text{Const.} \times F(8.99 \mu\text{m}) - 0.12 F(6.2 \mu\text{m}), \quad (\text{A2})$$

where the constant is the flux ratio $F([\text{Ar II}] 6.99 \mu\text{m})/F([\text{Ar III}] 8.99 \mu\text{m})$ and $F(6.2 \mu\text{m})$ is the 6.2 μm PAH flux.